MASTER THESIS REPORT

Materials science and engineering

3D-printed calcium phosphate scaffolds for bone regeneration
Impact of geometry and treatment
An in vivo study

Memory

Autor: M. Cyril Lehmann
Director: Prof. Maria Pau Ginebra
Co-Director: Prof. Montserrat Espanol
PhD Student: M. Santiago Raymond Llorrens
Call: Febrero 2020

Abstract

The combination of the direct ink writing (DIW) manufacturing technique, also named robocasting, with the use of self-setting calcium phosphate inks based on α-tricalcium phosphate opens new possibilities in the field of bone regeneration: i) On one hand, the DIW fabrication process allows a precise control on the external shape and internal porosity of the scaffold. The porosity allows the colonization of the bone tissue and the shape control opens new perspectives in personalised medicine; ii) On the other hand, the use of self-setting α-TCP inks provide a micro/nano porosity and a high specific surface area (SSA) to the bone graft. Both factors have been identified as crucial for the bioactivity of the material. Since the fabrication time is a crucial factor for the successful translation of these technologies to the clinical field, and the hardening reaction of conventional self-setting inks is slow, recent investigations have developed an alternative setting procedure (hydrothermal) that considerably reduces the hardening step from 7 days to 30 minutes.

Regarding the role of scaffold architecture in bone regeneration, it has been recently proved that the presence of concave surfaces enhances osteogenesis. However, since DIW is based on the extrusion of a paste through a needle, conventional DIW scaffolds are composed of extruded filaments with convex surfaces. Hence the interest in developing scaffolds with non-cylindrical strands, which have concave surfaces.

The aim of this study was to assess the in-vivo performance of calcium phosphate scaffolds, analysing on one side the effect of the setting treatment, i.e., comparing the biomimetic setting with the hydrothermal setting treatment, and on the other side comparing cylindrical vs. non-cylindrical strands. The characterization of the scaffolds obtained with the two different treatments revealed that whereas the biomimetic treatment resulted in calcium deficient hydroxiapatatite (CDHA), the hydrothermal treatment led to the presence of small amounts of β-tricalcium phosphate. Biomimetic scaffolds consisted of plate-like crystals, with higher SSA and smaller microporosity than the hydrothermal scaffolds, made of needle-like crystals. The geometry of the strands (i.e. cylindrical vs non-cylindrical) did not have an influence on the material composition, microstructure and global porosity, but they did have an impact on the mechanical properties, with lower ultimate compressive strength for the structures with non-cylindrical strands.

The scaffolds were implanted in the femoral condyles of 10 adult female New Zeeland rabbits and explanted after 8 weeks. The samples were embedded in resin and characterised by micro-computed tomography, scanning electron microscopy and optical microscopy after Golden-Mason trichrome staining. All the samples presented the formation of new mature lamellar bone and a successful osteointegration. No statistically significant differences were observed between the samples studied in terms of the amount of newly formed bone, quantified from the SEM observation. Micro-CT allowed the assessment of bone formation in 3D, although difficulties related to image processing prevented the volumetric quantification that might have revealed significant differences. However, a clear tendency was found for new bone formation in constrained microenvironments, such as the contact zone between two strands or the concavities present in the non-cylindrical condition. Further data analysis will have to be carried out to assess the differences in the different sample conditions.

Keywords : Bone, regeneration, scaffold, calcium phosphates, ceramic, concave, strands, alpha tricalcium phosphate, α-TCP, calcium deficient, hydroxyapatite, CDHA, biomimetic, 3D printing, robocasting, direct ink writing, DIW, non-cylindrical.

Acknowledgments

Glossary

HA : Hydroxyapatite
CaP : Calcium phosphate
CDHA : Calcium deficient hydroxyapatite
TCP : Tricalcium phosphate
DIW : direct ink writting
BMPs : Bone morphogenic proteins
CPC : Calcium phosphate cement
MSC : Mesenchymal stem cells
SSA : Specific surface area
µ-CT : Micro computerised tomography
SEM : Scanning electron microscopy
ROI : region of interest

Index

1. Preface

1.2. Origin of the work

The current work is on the continuity of previous works of the Biomaterials, Biomechanics and tissue engineering research group (BBT) of the UPC, and more precisely the continuity of two previous PhD thesis. On one hand Yassine Maazouz's thesis showed that it is possible to develop CaP scaffolds using self-setting CaP inks. On another hand, Albert Barba's thesis showed that the geometrical properties and more specifically the presence of concave surface, play a critical role in osteogenesis.

1.3. Motivation

As part of a French engineering diploma, this master thesis is the opportunity to understand the organization and the requirements of the fundamental research. It is also the opportunity to acquire research skills, such as organization and experiment planning with the master of characterization techniques. Finally, this work is the opportunity to acquire precise knowledge in the biomaterial sector, and more precisely in the bone regeneration sector, exploring the possibility to obtain CaP scaffolds with concave surfaces and the effect on osteogenesis in vivo.

1.4. Requirements

The project calls for the implementation of scientific experimentation using the technical and technological means proposed by the UPC for the characterization of materials as well as in-vivo characterization.

2. Introduction

Bone is continuously subjected to a process of remodelling, replacing old tissue with new tissue. Indeed, bones are composed of cells called osteocytes surrounded by an extracellular matrix which is renewed thanks to the action of two cell types: the osteoblasts which synthesize the bone matrix, and the osteoclasts which resorb aged bone tissue. This process is called bone remodelling and gives to the bone self-repairing proprieties. Bone remodelling is a constant process able to self-regulate its formation and resorption in order to obtain a balanced equilibrium thanks to osteocytes which act as mechanical sensor. In that sense, the lack of use of a bone leads to its resorption and traumatic events such as bone fracture lead to an acceleration of the bone regeneration. In other terms, bone has the capacity to adapt itself to external factors, such as physical activity or injuries. However, this natural process of self-repair has his limits: mechanical or biological problems as well as certain pathologies and surgical interventions with significant bone loss make the natural osteogenesis inefficient. In fact, above a critical size of the defect, the bone layer by layer remodelling process is not able of bridging the gap. Then, there is here the need of a structure that serves as a support to bone cells to regenerate the bone, which is called a bone graft. [1]

2.1. Bone grafts

The bone formation or osteogenesis, the process of laying down new bone material by osteoblasts, depends on different proprieties of the bone graft. One of the most important is the biocompatibility of the graft, that is to say the property of not having toxic or injurious effects and not producing immunologic response in living tissue. [2]. Different degree of biocompatibility exists, but regarding the long stay of the bone graft into the body, the material chosen has to be highly biocompatible. The osteoconductivity, defined as the facilitation of blood vessel incursion and new bone formation into the passive surface of the graft, is another property of the graft that influences the formation of new bone. Finally, the capacity of the graft of creating new bone thanks to the differentiation of surrounding mesenchymal stem cells into osteoblasts, the osteoinduction of the graft, is the last main property that can be analysed. [3]

The first solution ever considered regenerating bone when the process of natural regeneration is not sufficient, were the bone autografts. This technique consists in harvesting

bone tissue from another anatomical location of the same patient. The cancellous part of the graft will provide a reservoir of stem cells capable to produce bone tissue on the damaged site. Because the transplanted tissue comes from the patient, there is no immune response. The success of the autograft partly depends on the graft's vascularization which is necessary to provide nutrients and then enable the production of new bone cells. A big inconvenience of this technique is that a double surgical operation is required: one for harvesting the bone graft and the other one for grafting the extracted bone in the treated defect. This additional surgery can cause different complications, such as pain or abscess. Furthermore, another limit to this process is the size limitation of the graft.[4]

Allografts appeared as an alternative that used tissues from a donor (usually cadaver or from total hip replacement) to overcome the inconveniences of autografts. This technology requires an important treatment of the tissue in order to avoid the immune rejection: elimination of blood stem cells, endothelial cells or even cartilage cells. In this sense, this graft acts only as a guide on which the bone can grow, and is not osteogenic such as autograft. Bone grafts deriving from different species are called xenografts. Mainly bovine, porcine or equine origin has been used as bone graft. Because the graft is subjected to high immune response or viral contamination, a multi-step treatment is done, including removal of cellular debris, deproteinization, viral inactivation and sterilization [5] .Finally, only the mineral part of the bone is kept and will provide, like the allograft, a framework for the bone to grow. The main advantage of allograft and xenograft is that the surgery for harvesting the bone graft, with its potential complication, is avoided. On the other hand, the lack of osteogenesis and osteoinductive properties make the bone regeneration less efficient. Furthermore, ethical and religious concerns can be generated by these processes. [6]

Synthetic bone grafts open new perspectives in the field of bone regeneration. The absence of disease transmission, avoidance of additional surgeries and the unlimited source of material give synthetic bone grafts huge advantages. Furthermore, these materials can be chemically and physically tuned to offer optimal mechanical and biological features. Different synthetic materials are investigated or even commercialised for this use, such as ceramic based materials (i.e. calcium sulfates and calcium phosphates) [6]   or polymers/ceramics (i.e. polycaprolactone) [7].

Synthetic materials can be used as graft in different conformations. Granules can be of use in case of a confined defect, but they are not mechanically stable. On the other hand, standard blocks provide a high stability, but there is a need of being shaped during the surgery,

meaning a low accuracy in the grafts shape. Minimally invasive injectable materials can also be used for confined defects. The development of additive technologies leads to new perspectives for the fabrication of bone substitutes. These technologies allow to create personalised grafts for specific patients. Furthermore, the stability of these grafts is high and there is the possibility of loading them. The direct ink writing (DIW) technique, consisting in dispensing layer by layer an ink with tailored rheological properties, allows the customization of the bone graft as well as the control of its porosity and its structure. The ink composition plays a key role on the control of the physicochemical properties. [8]

In order to improve the osteoinduction of synthetic bone grafts, investigations were made to combine the scaffold with cells and growth factor, in particular with the presence of exogenous bone morphogenetic proteins (BMPs). Even if investigations are still in process, this technology raises ethical, logistical and economical concerns that leads to a high diminution of the use of BMPs at a commercial level. [9] Alternative research lines are being done focused on controlling the composition and physicochemical properties such as structure, porosity and SSA in order to improve osteocondution, in which the current project is part of.

2.2. Calcium phosphates

Historically, calcium phosphates (CaP) are used since the 70s as a synthetic support of bone regeneration for their similarity of composition to the mineral phase of bone. [10] Furthermore, this material presents relevant properties, such as an excellent bioactivity, osteoconductivity and the capacity of being resorbable. [6] Among the sintered CaP ceramics, hydroxyapatite (HA) $Ca_{10}(PO_4)_6(OH)_2$, beta-tricalcium phosphate (β- TCP) $Ca_3(PO_4)_2$ and biphasic calcium phosphate (BCP), a combination of HA and β- TCP, are the most widely used synthetic bone substitutes. But the high crystallinity and the lack of nanostructure of these sintered ceramics differ from the low-crystallinity, non-stoichiometric structure and calcium-deficient form of the natural bone [11].

Biomimetic routes based on the self-setting reaction of calcium phosphate cements (CPCs) have been studied to overcome the limits of classical sintered ceramic. The most common calcium phosphate formulation is based on the hydrolysis of α- tricalcium phoshpate (α-TCP) $Ca_3(PO_4)_2$ to calcium deficient hydroxyapatite (CDHA) according to the following equation :

$$3\ Ca_3(PO_4)_2 + H_2O \rightarrow Ca_9(PO_4)_5(HPO_4)OH$$
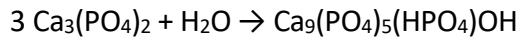
These investigations resulted in a calcium deficient hydroxyapatite (CDHA) characterised by having a low-crystallinity, a non-stoichiometric structure and being a nanostructured material. [12]

The self-setting reaction of calcium phosphate, leading to a nanostructured material, opens new perspectives in bone regeneration. Indeed, the nanostructure influences the interaction between the material and the tissue. Investigations have been made to understand the complexity of this interaction and, even if the mechanism is not clear, some proprieties have been found as key factors for the osteoinduction, such as the microporosity or the specific surface area (SSA). A recent investigation concludes that nanostructured biomimetic materials, with high SSA and porosity on the micro and nanoscale, promote some mechanism for osteoinduction such as the entrapment of growth factors or relevant proteins and the release of calcium and phosphate ions. [13] Furthermore, the macrospore's geometry has a huge impact on the performance of the scaffold: concave macropores provide confined spaces acting as an adequate microenvironment for the differentiation of MSCs allowing a better osteogenic capacity than macropores with convex geometry. [13] [14] The degradation of the scaffold play also a key role in osteoinduction. CDHA scaffolds are progressively resorbed by the osteoblastic activity and replaced at the same time by new bone, whereas in the case of sintered HA, the bone is only deposited on the surface of the scaffold [9]. The high resorption rate of CDHA, due to its high SSA, low crystallinity and lack of stoichiometry, is explained by the activity of multinucleated osteoclast-like cells leading to secretion of osteogenic growth factor able to trigger MSC differentiation able to stimulate the bone formation [13]. Other sintered calcium phosphate, such as β-TCP, are also quickly degraded by a dissolution in the basic environment but acts like a passive degradation: the non-synchronization between scaffold degradation and new bone formation leads to a loss in the scaffold functions [15] [16] [17]

2.3. Development of CaP scaffolds by direct ink writing with self-setting inks

The manufacturing of CDHA scaffolds with DIW presents a very promising future: Allowing to combine the biomimetic properties of this material (i.e. similar composition to natural bone, high specific surface area and high interaction with the host tissue, active

regeneration etc.) with all the advantages of an AM mild process (i.e. control of the pore size and geometry allowing to obtain an homogeneous and interconnected pore network, control of the scaffold's shape allowing to fabricate patient-specific products for reconstruction of complex geometries and combination with virtual surgical planning). The last works has led to a fast manufacturing process that technically ready to be directly transferred to the clinics opening new perspectives in bone regeneration strategies.

Different formulations of low temperature self-setting inks were developed [18], avoiding the consolidation by harsh techniques such as sintering at high temperature and its effect on chemical and structural properties of the final scaffold. These calcium phosphate inks are composed of alpha-tricalcium phosphate (α-TCP) combined with different binders such as gelatin [19], type I collagen [20] or poloxamer p407 [21] others. The hydrolysis reaction of α-TCP into a calcium deficient hydroxyapatite (CDHA) acts as the hardening process of the ink and leads to the formation of micro and nanostructured crystals similar to the mineral phase of bone, which are not reached with the classical sintering process. This biomimetic approach result in an enhanced bioactivity of the scaffold but, on the other hand, the mechanical entanglement of CDHA nano-crystals present considerably lower mechanical properties than the classical sintered stoichiometric HA.

In previous research, an ink was developed based with a poloxamer P407 (Pluronic F127) aqueous solution as binder [8]. Poloxamers are synthetic polymers that exhibit thermoresponsive behavior, with a finely tunable $T_{sol-gel}$. Poloxamer P407, an ethylene oxide and propylene oxide block copolymer, is among the most commonly used poloxamers due to very interesting rheological and biological properties. [21]. This poloxamer has been widely studied in DIW applications for both hydrogels for bioinks and as binder for powder suspensions /slurries due to its shear-thinning rheological properties. Previous investigations demonstrated that its inverse thermal gelling properties made it very suitable for its use in injectable αTCP suspensions as it can handle a post-printing biomimetic treatment (37ºC for 1 day 100%RH followed by 6 day immersed in water) when hydrogels with traditional thermal gelling properties (i.e. gelatin) would melt. [22]

The traditional hydrolysis reaction of the biomimetic process took a total of 7 days to complete. The scaffold is printed on a thin plastic sheet and put inside a sealed Tupperware with distillate water 15 minutes after being printed. The system is placed in an incubator at 37° for 24 hours to perform the pre-hardened phase. Then, the hardened phase is carried out by changing the distilled water and placing the system again in the incubator at 37° for 6 days. Such a long

time span hampered the translation to the clinic. For this reason, investigations were made to develop an alternative process with reduced duration. The most relevant alternative process was named hydrothermal-immersed process. The scaffold is printed with the same conditions on a thin plastic sheet. The step of pre-hardened consists in placing the printed scaffold in an autoclave previously heated at 121° with water to allow steam saturation for 6 minutes. Next, step of hardening consists of placing the pre-hardened scaffolds in distilled water and placing them in an autoclave at 121°C at 2 abs. atm pressure for 30 min. [8] This alternative method was claimed to maintain the biomimetic features as the main key-characteristics of these materials were found. Nevertheless, slight differences were found in key the physicochemical properties (i.e. composition, microstructure, specific surface area, porosity and compressive strength) but the in-vivo performance of these two treatments was not compared.

Studies have been carried out on the print head used in the DIW process in order to obtain filaments with a geometry other than cylindrical.In this regard, non-cylindrical filaments can be obtained with new process of microfabrication by deposition [23]. Indeed a custom modular nozzle designed with a CAD software (SolidWorks, Dassault systemes, Vélizy-Villacoublay, France) and lathed in Polyether ether ketone (PEEK) allows to obtain a non-cylindrical nozzle shape (Figure 1.a). The final shape obtained after this innovative process (Figure 1.b) opens up the possibility of printing scaffold with a non-cylindrical filament shape. With this new technology, parts of the strand present a convex geometry. However, this convexity is less important than the one presents in the foamed scaffold.
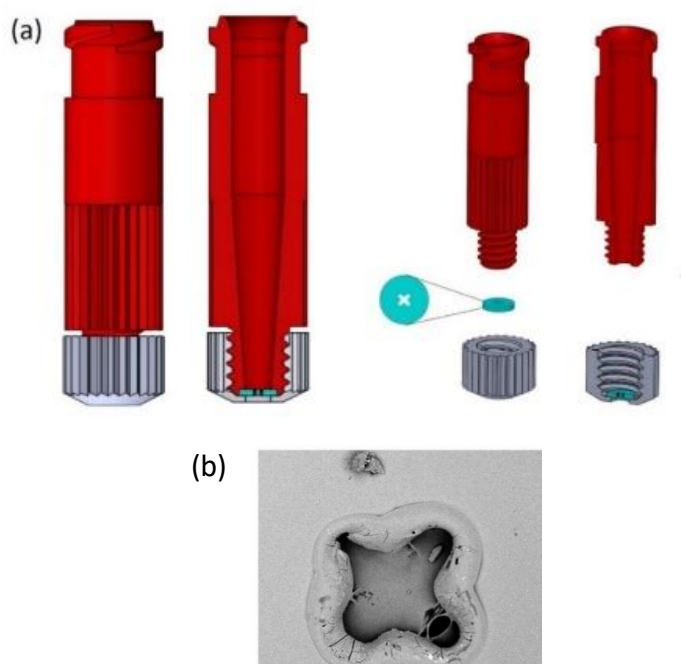

Figure 1 : a) Schema of the custom modular nozzle design. (b) SEM images of resulting disc orifice.

2.4. In vivo characterisation of the osteogenic potential

The biological features of biomimetic 3D printed scaffolds was assessed and compared to foamed scaffold with the same composition by Barba et al. in an in-vivo study in beagle breaded dogs. [14] Cylindrical scaffolds of different conditions, CDHA foamed scaffold and two CDHA robocasted scaffolds (3D) with different inner diameters (450 and 250 µm) were implanted in both ectopic and orthotopic locations. The study concluded that both CDHA robocasted and foamed scaffolds presented similar results in orthotopic defects, demonstrating its osteo-conductive properties. However only the CDHA foamed scaffold was capable of generating ectopic bone whilst the CDHA robocasted scaffold just show small sights of bone formation in the strand crossing corners. The osteoinductive properties of CDHA foamed scaffold was explained by the presence of concave porosities in its microstructures that may lead to confined spaces acting as an adequate microenvironment for the differentiation of MSCs.

In-vivo performances of the fast hydrothermal-immersed treatment has never been validated. Moreover, only the classical DIW technique with cylindrical geometry, leading to a scaffold with a convex geometry, has been tested with in-vivo conditions. Indeed, the new process for obtaining a non-cylindrical geometry has never been tested under in-vivo conditions. The current project, whose objectives will be explained in section 2.5, is a continuation of the in vivo experimentation by Alber Barba et al. The design, implanting and explanting steps were carried out before this current project by M. Santiago Raymonds and Prof.Maria Pau Ginebra. It is important to say that all animal procedures in this study were performed in compliance with the Guide for Care and Use of Laboratory Animals [24] and the European Community Guidelines (Directive 2010/63/EU) for the protection of animals used for scientific purposes [25] and under the permission of the local Animal Ethics Committee for Human and Animal Experimentation (Approval # CEAAH 4683).

Many animals are used in in-vivo studies due to their similarities to human, such as mice, dogs and rabbits. The defect area for bone regeneration is also important depending on the study. This present study was performed on twelve adult female New Zealand rabbits with a weight range of 4.8–5.5 kg and an age range of 8–12 months. The bone defects was created by drilling in the both femoral condyles of the rabbit and different scaffold, allowing to assess the different shape and treatment performances, were set up. The animals were euthanised two months (8 weeks) after the surgical procedure according to the legislation of the American Veterinary Medical Association (AVMA). Figure 2 shows the images of the operation. All of this

procedure was done before the study was initiated and was not an integral part of the current study. The surgical procedure is detailed in appendix 1.
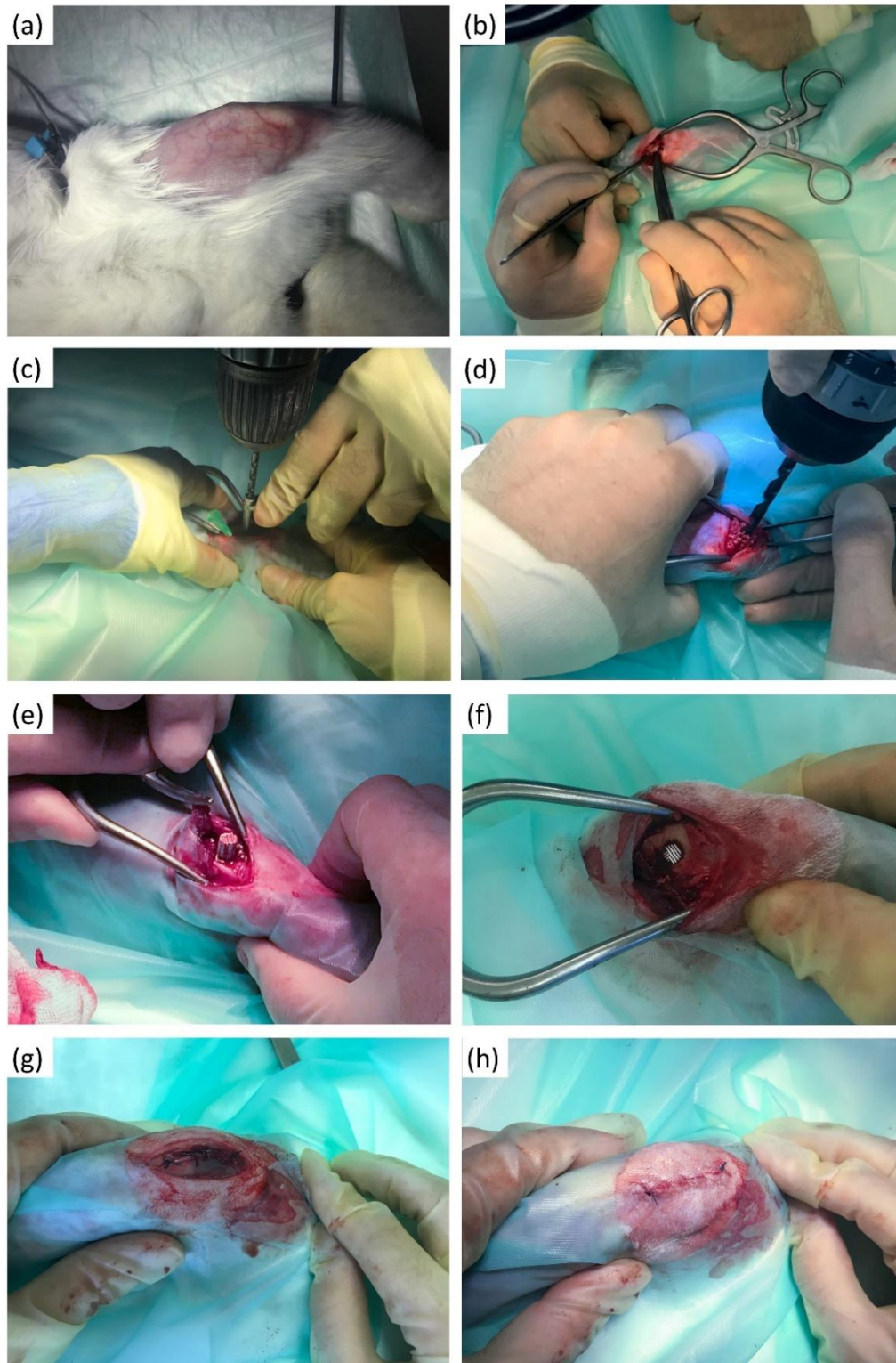

Figure 2 : (a) Defect region pre-operatory preparation. (b) Medial parapatellar incision in the femoral condyle. (c) 2.5mm drilling in the centre point of the medial aspect of the femoral condyle guided by a drill guide. (d) Expansion of the initial guide hole to 5mm. (e, f) Press fit grafting of the cylindrical scaffold. (g) Suture of the joint capsule. (e) Suture of the skin.

2.5. Objectives

This study analyse the in-vivo performance of biomimetic 3D printed scaffolds, focusing on the effect of:

i) Strand morphology

ii) Post-printing process (biomimetic and hydrothermal)

This will be achieved with two specific objectives:

A) Characterisation of the scaffolds previous the implantation

B) Histomorphometry and histological characterisation of the explanted samples after 8 weeks implanted in rabbit

To assess the in-vivo performance of the graft, histology and Micro computed tomography (µCT) techniques are used to evaluate the performance of the scaffold. Micro-CT allows a 3D reconstruction and the SEM technology leads to images with high resolution. To assess bone formation inside the scaffold, these to techniques are combined, avoiding a subjectivity during the differentiation between bone and scaffold. [26]

To reach these objectives, three different scaffolds will be compared: one cylindrical obtain with biomimetic treatment "Biomimetic Cylindrical" (B-C), another cylindrical obtain with hydrothermal treatment "Hydrothermal Cylindrical" (H-C) and the last one non-cylindrical obtain with hydrothermal treatment "Hydrothermal Non Cylindrical" (H-NC).

3. Materials & methods

3.1. Materials

The material obtained from the beginning of the project to carry out the summer study:

- Calcium deficient hydroxyapatite scaffolds.

  Some of the scaffolds have already been prepared and others were prepared during the project. The CDHA scaffolds were prepared according to a method based on the hydrolysis of alpha-tricalcium phosphate (α-$Ca_3(PO_4)_2$, α-TCP) [13]. All the fabrication was carried out in an ISO 7 cleanroom (Facilities of Mimetis Biomaterials SL).

  As explained in the objectives, three conditions of scaffolds were investigated in the study. Each one has a different geometry/post-printing treatment combination in order to reach the objectives. The table 3 summarised these two mains characteristics.

Table 1 : Main characteristics of the scaffolds

Name	H-C	B-C	H-NC
Geometry	Cylindrical	Cylindrical	Non cylindrical
Treatment	Hydrothermal	Biomimetic	Hydrothermal

- Explanted scaffolds

  18 samples from rabbits after their euthanasia, containing the implanted scaffolds and a part of the femoral condyle, were brought to the laboratory to start the histomorphometry and histological analyses. Table 2 illustrates the random distribution of conditions that occurred prior to this current study.

Table 2 : Summary of the condition and the name of the scaffold implanted in every site

Animal	Femur condyle		Observations
	Left	Right	
1	H-C 5	H-NC 8	N/A
2	H-NC 11	H-C 2	N/A
3	H-C 3	B-C 5	N/A
4	B-C 2	H-C 1	N/A
6	H-C 24	H-NC 13	Drop Out
7	H-NC 3	H-C 4	N/A
8	H-C 7	B-C 6	N/A
9	B-C 7	H-NC 5	N/A
10	H-NC 9	B-C 10	N/A
11	B-C 8	H-NC 1	N/A

- Alpha tricalcium phosphate (α-TCP) powder

The powder was also characterised to complement the data obtained in previous works. The powder obtained directly after manufacture as well as the powder that has undergone a sieving step to avoid problems of print head clogging, have been characterized as follows

3.2. Raw material characterization

Alpha tricalcium phosphate (α-TCP) powder (Innotere TA2, Batch: 037-127-TA) Powder used for printing scaffolds was sieved by vibration with a 40 µm stainless steel mesh sieve (Filtra, IRIS FTL-0200). Powders where characterised with the following techniques:

- XRD :

The diffractometer (D8 Advance, Bruker) equipped with a Cu Kα X-ray tube was operated at 40 kV and 40 mA. Data were collected in 0.02°/step over the 2θ range of 10– 80° with a counting time of 2 s per step. Phase quantification was performed using the reference intensity ratio method (EVA, Bruker) comparing diffraction patterns of the crystalline structures of α-TCP (ICDD PDF 00-029-0359), CDHA (ICDD PDF 01-086-1201) and β-TCP (ICDD PDF 00-003-0681).

- PSD

The particle size distribution was measured for two alpha TCP preparations, one sieved at 40um and one unsieved. This characterization allowed the control of the particle size distribution of the powder as well as the effect of sieving. The results obtained with the Mastersizer 3000 (Malvern panalytical, Malvern, UK) was treated with the mastersizer software (Malvern panalytical, Malvern, UK)

- SEM

The microstructure of the α-TCP powder was observed under a DESKTOP SEM field emission scanning electron microscope (PhenomXL, Phenomworld, ThermoFischer scientific) at 15 kV with BSD and SED detector at a magnification of 2 000 and 10 000, after coating the surface with a thin carbon layer.

3.3. Characterisation of pre implanted scaffold

3.3.1. Macrostructure

3.3.1.1. SEM

Cross section and top view of the scaffolds was observed under a field emission scanning electron microscope after a sputter deposition with carbon (Phenom XL, Phenom world, ThermoFischer scientific) at 10kV with SED detector at a magnification of 500 and with a mapping scan (Automated image mapping software, Phenom ProSuite, PhenomXL, Pehnom World) with a magnification of 350, an overlapping of 5% and an averaging of 8.

3.3.1.2. uCT

X-ray computed microtomography (μCT) analysis was conducted using the Bruker Skyscan 1272 system equipped with a detector CCD, 11Mp, 14-bit cooled CCD fiber-optically coupled to scintillator, 100 kV/10 W/250mA maximum power. The tomographic measurement was performed with an acceleration voltage of 100 kV and an X-ray current of 100 μA. The X-ray spectrum of tungsten target was modified by using a 0.11 mm thick cupper filter. The exposure time per projection was 1650 ms and 1800 projections were taken around 360°. The isotropic linear voxel size (voxel resolution) of the obtained volume was 18μm. The sample tomographic reconstruction was performed with NRecon software (Micro photonics inc), using the object shifting correction and the beam hardening correction in the different material modes. The visualization of the samples, as well as the structural parameter quantifications, were performed using CTVox software (3DSuite software, Bruker).

3.3.2. Microstructure

The microstructure of the scaffolds fabricated with the three different conditions was observed under a desktop scanning electron microscope (Phenom XL, Phenom world, ThermoFischer scientific) at 10kV with SED detector at a magnification of 2 000 and 9 000 after a sputter deposition with carbon.

3.3.3. Chemical characterisation

3.3.3.1. XRD

Phase composition of the different scaffold was assessed by X-ray powder diffraction on powder obtained for each scaffold after grinding in an agata mortar. The diffractometer (D8 Advance, Buker) equipped with a Cu Kα X-ray tube was operated at 40 kV and 40 mA. Data was collected in 0.02° step. Phase quantification was performed using the reference intensity of the crystalline structure of α-TCP (ICDD PDF 00-029-0359), CDHA (ICDD PDF 01-086-1201) and β-TCP (ICDD PDF 00-003-0681) with EVA software (EVA, Bruker).

3.3.3.2. FTIR

Attenuated Total Reflectance of Fourier-transform infrared (ATR-FTIR) spectroscopy analysis was performed in a Nicolet 6700 FTIR. Spectra were recorded in the 4000 to 675 cm-1 range, at 256 scans accumulation and 3.8 cm-1 resolution. The results obtained were treated with a base-line correction to remove noise.

3.3.4. Specific surface area

The specific surface area (SSA) was determined by nitrogen adsorption using the BET (Brunauer-Emmett-Teller) method (ASAP 2020, Micromeritics). Prior to measurement, samples were outgassed in vacuum conditions (10 mmHg) at a holding temperature of 100 °C for 2 h.

3.3.5. Porosity

3.3.5.1. Skeletal density

The skeletal density of the scaffolds (ρ_{skel}) was assessed by helium pycnometry (AccuPyc 1330, Micromeritics, USA). The experimentation was done with grind sample for each condition with an approximate volume of 0.2 cm^3. An iron ball of 2.43cm^3 was used to complete the volume of the chamber of 3.5cc.

3.3.5.2. Apparent density and total porosity

The apparent density of the scaffolds (ρ_{app}) was calculated as the quotient of the scaffold mass over the scaffold equivalent cylinder volume obtained from the measurements of the scaffold dimension. Cubic blocks have been manufactured and polish to replicate the same implantation condition. Before measuring, the scaffold was dried at 60° overnight. The dimension was measured with a digital caliper (0-200mm, Fervi) and the weight was measured with a high precision digital balance (Cobos precision ATX-224).

The value of the total porosity (P_{TOT}) was calculated with the equation (1) :

$$P_{TOT} = \left(1 - \frac{\rho_{app}\left[\frac{g}{cm^3}\right]}{\rho_{skel}\left[\frac{g}{cm^3}\right]}\right) \times 100 \quad (1)$$

3.3.5.3. Pore entrance size distribution

Pore entrance size distribution of the open porosity were analysed in the range between 0.006 and 360μm by mercury intrusion porosimetry (MIP, AutoPore IV Micromeritics). The volume of nano - micropores normalised per unit of mass (Vmicro) was measured from the sum of the incremental mercury intrusion in the pores smaller than 10μm.

3.3.5.4. Porosity percentual distribution

3.3.5.4.1   uCT assessed (Macro-Porosity)

The macrostructure analysis by uCT allows, using CTan software (3DSuite software, Bruker), to calculate the macroporosity of each scaffold. To allow this analysis, the reorientation along the longitudinal axis had to be performed with the CTVox software (3DSuite software, Bruker) and a region of interest (ROI) was defined for each scaffold. To limit the induced subjectivity, the region is delimited for all the scaffolds by an oval geometric shape (initial shape of the scaffolds) with as limit the perimeter of the scaffolds.

3.3.5.4.2   Indirect porosity (Micro- & Macro-Porosity)

Porosity was calculated by an indirect method, combining several measurements: apparent density (3.4.5.3), MIP results and skeletal density (3.4.5.4). [27].

The value of the micro porosity (P_{micro}) was calculated with the equation (2). The value of V_{micro} comes from the MIP results :

$$P_{MICRO} = \left(V_{MICRO}\left[\frac{cm^3}{g}\right] \times \rho_{app}\left[\frac{g}{cm^3}\right]\right) \times 100 \qquad (2)$$

Finally, the value of macro porosity (P_{macro}) was calculated with the equation (3):

$$P_{MACRO} = P_{TOT} - P_{MICRO} \qquad (3)$$

3.3.6. Mechanical characterisation

The compressive strength of the different scaffolds was measured with a universal testing machine (Bionix 858 uniaxial, MTS) at a speed of 1mm/min until fracture. The three different treatments of scaffolds, B-C, H-C and H-NC have been tested in two conditions: non-polished and polished, in wet conditions. All the scaffolds was printed with a cubic geometry of 8x8x8mm. The ultimate compressive strength (UCP) as well as the Young's modulus are the two mechanical properties focused on the study. The polishing step opens up the porosity and removes the outer layers of the scaffold which, for reasons of technological feasibility, are denser than the rest of the scaffold.

3.4. Characterisation of explanted scaffold

3.4.1. Sample harvesting and processing

3.4.1.1. µCT acquisition

After explantation of the condylar areas, the samples were fixed in 4% neutral buffered formalin solution for two weeks. Then the samples were dehydrated in an increasing series of ethanol solutions. Then, samples were analysed by X-ray µCT using the Bruker Skyscan 1272 system equipped with a detector CCD, 11Mp, 14-bit cooled CCD fiber-optically coupled to scintillator, 100 kV/10 W/250mA maximum power. The tomographic measurement was performed with an acceleration voltage of 90 kV and an X-ray current of 111 µA. The X-ray spectrum of tungsten target was modified by using a 0.5mm thick aluminium filter and a 0.038mm thick cupper filter. The exposure time per projection was 2300 ms and 1800 projections were taken around 360°. The isotropic linear voxel size (voxel resolution) of the obtained volume was 9µm. The sample tomographic reconstruction was performed with NRecon software (Micro photonics inc), using the object shifting correction and the beam hardening correction in the different material modes. The visualization of the samples, as well as the structural parameter quantifications, were performed using CTVox software (3DSuite software, Bruker).

3.4.1.2. Embedding, cutting and polishing process

Then, the embedding of the sample was done with different graded mixtures of ethanol and methyl methacrylate resin (Technovit 7200, HeraeusKulzer GmbH, Hanau, Germany) in dark conditions due to the photosensibility of the resin. The protocol is summarised in the table 3. The agitation was carried out by Rotamax ® 120 at a speed of 75rpm and the vacuum was executed with a vacuum bell jar system with a diaphragm vacuum pump (Comecta, GM-0.5) at 0.08 MPa.

Table 3 : Embedding process

Ethanol%/resin%	75/25	50/50	25/75	0/100	0/100
Condition	agitation	agitation	agitation	agitation	vacuum
Recipient	30ml PP container	30ml PP container	30ml PP container	30ml PP container	Mold
Time (days)	2d	2d	2d	2d	3d

The embedded samples were subsequently photopolymerised in molds for 12 hours under UV light with the Exakt 520 UV machine (EXAKT Advanced Technologies GmbH, Norderstedt, Germany) followed by 12 hours under white light (Figure 3.a). The resulting blocks are depicted in Figure 3.b. The blocks were cut in two along the longitudinal axis of the implant with a precision band saw (EXAKT Cutting System, EXAKT Advanced Technologies GmbH, Norderstedt, Germany) in order to analyse the region of the scaffold with a biggest scaffold cross section. Prior and after this cut, two parallel cuts were made on both sides of the scaffold (Figure 3.d). The resulting blocks containing both sides of the scaffold were stuck to a PMMA 3mm thick sample holder (Figure 3.c) with double side tape with the scaffold facing up. Then, the samples were polished (EXAKT Grinding System, EXAKT Advanced Technologies GmbH, Norderstedt, Germany) with water sandpaper disc of 250mm and grain size P1200 and P4000.
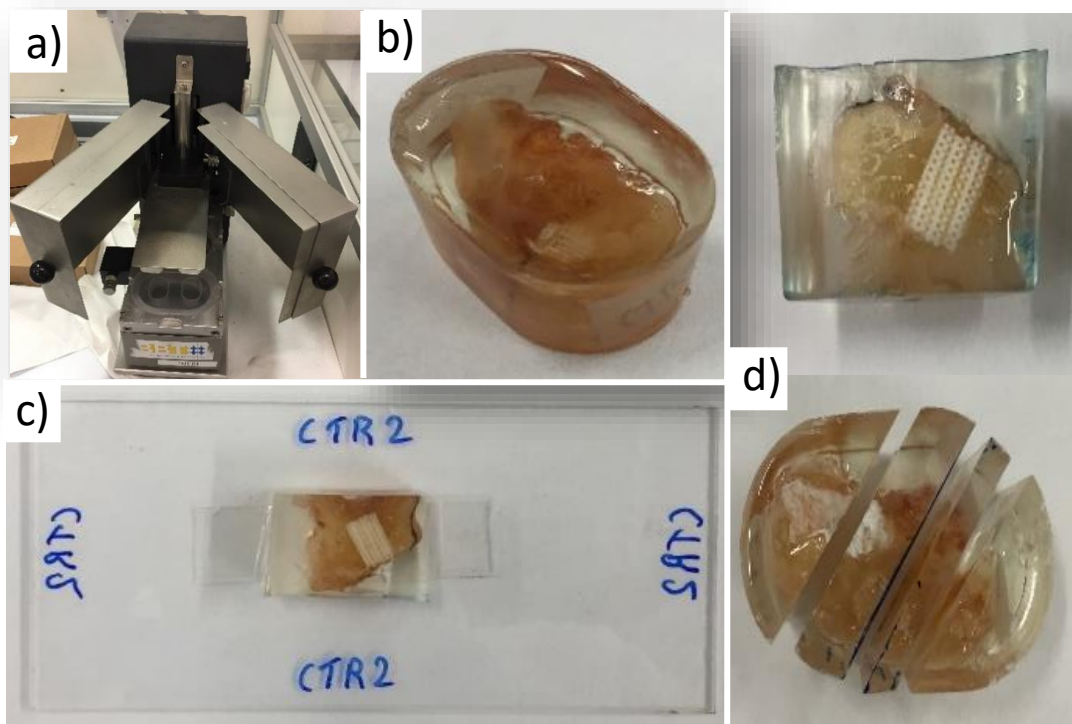
Figure 3 : (a) Exakt UV machine ermitting the photopolymerization. (b) Block of resin photopolymerised. (c) Scaffold stuck on a PMMA plate for polishing treatment. (d) Parallel cut of the block.

This process concluded with two samples per scaffold.

3.4.1.3. SEM acquisition

The first sample was then coated with a thin carbon layer by a sputter deposition and a tilt scan SEM image (cf 3.4.2.1 for condition) was carried out to obtain a global view of the cross section.

3.4.1.4. Histological staining process

The second sample for each scaffold was glued through the polished side to a second transparent PMMA sample holder with a transparent resin (Technovit 7210 VLC, HeraeusKulzer GmbH, Hanau, Germany) by 15 minutes of UV polymerisation (Exakt 402 UV machine, EXAKT Advanced Technologies GmbH, Norderstedt, Germany). Then, a cut at 800um from the plate was carried out with a precision band saw (EXAKT Grinding System, EXAKT Advanced Technologies GmbH, Norderstedt, Germany). After, samples were polished (EXAKT Grinding System, EXAKT Advanced Technologies GmbH, Norderstedt, Germany) with water sandpaper disc of 250mm and grain size P1200 until reaching 250-150 µm with a digital capiler (0-25mm, Fervi) and, after, with P4000 grain

to finally reach histological sections of around 80-100 µm. Finally, samples were stained with Goldner-Masson-trichrome process for histological evaluation with a series of reagent manufactured by Merck KGaA, germany :

- Cleaning with an ethanol-acetone 1:1 solution to open the pores of the samples.
- Submerged the samples in Harris hematoxylin solution at 70°C for 15min.
- Cleaning with tap water until obtain clear water.
- Submerged the sample in Azophloxine solution at ambient temperature for 7 min.
- Submerged 3 times the samples in acetic acid (2%vol).
- Submerged the sample in tungstophosphoric acid orange G solution at ambient temperature for 5 min.
- Submerged 1 time the samples in acetic acid (2%vol).
- Submerged the sample in light green SF solution at 40° for 5 min.
- Submerged 1 time the samples in acetic acid (2%vol).
- Cleaning with tap water until obtain clear water.
- Submerged 1 time the samples in distilled water for 15 min

The evaluation of the histology was processed by a light microscopy (see 3.4.2.1).

3.4.2.   Histomorphometry and histology assessment

3.4.2.1. 2D anlysis – SEM and staining

The 2D evaluation of bone formation was performed using SEM images with an automated image mapping software (Phenom ProSuite, PhenomXL, Pehnom World). SEM was operated with a beam intensity of 10kV, the BSD detector, a magnification of 350, an overlapping of 5% and an averaging of 8.). A region of interest (ROI) was defined for each cross-section and a segmentation based on grey intensity was performed by the software Ilastik, a machine learning software, to separate the three parts: bone, scaffold and resin. To assess the bonne formation equally between the different cross sessions, the bone formation was assessed on the available area of the images with the equation (4):

$$\% \ new \ bone \ on \ available \ area = \frac{new \ bone \ area}{total \ area - scaffold \ area} \ x \ 100 \quad (4)$$

The histological analysis of the staining step was performer with the BX51P polarizing microscope (Olympus corporation, Tokyo, Japan) at two magnification; 20 and 50; ans was treated with the analySIS docu (Olympus soft imaging solution, Tokyo, Japan) software This analysis allows the shade of the bone formed to allow a qualitative analysis, such as the analysis of the mechanism of bone formation or the morphology of the bone.

3.4.2.2. 3D analysis – Image processing

The 3D evaluation of bone formation was performed using a method combining the use of SEM and micro-CT.

The micro-CT data of each sample was reconstructed by a software program, NRecon (Micro photonics inc), with the objective of allowing grey level differentiation of bone, scaffold and the rest. To avoid a subjective analysis with an arbitrary threshold definition, the analysis was complemented by the SEM image obtained on the same sample. The objective is to find the same cross-section of the SEM image on the micro-CT. Since the SEM image has a much higher resolution, it allows the three parts to be precisely differentiated. The segmentation done by machine learning with the software Ilastik (Figure 4) allows to differentiate the three different components of the sample in the region of interest (ROI): the bone (Figure 4.B), the scaffolds (Figure 4.C) and the soft tissue part (Figure 4.D). Three binary images are obtained.
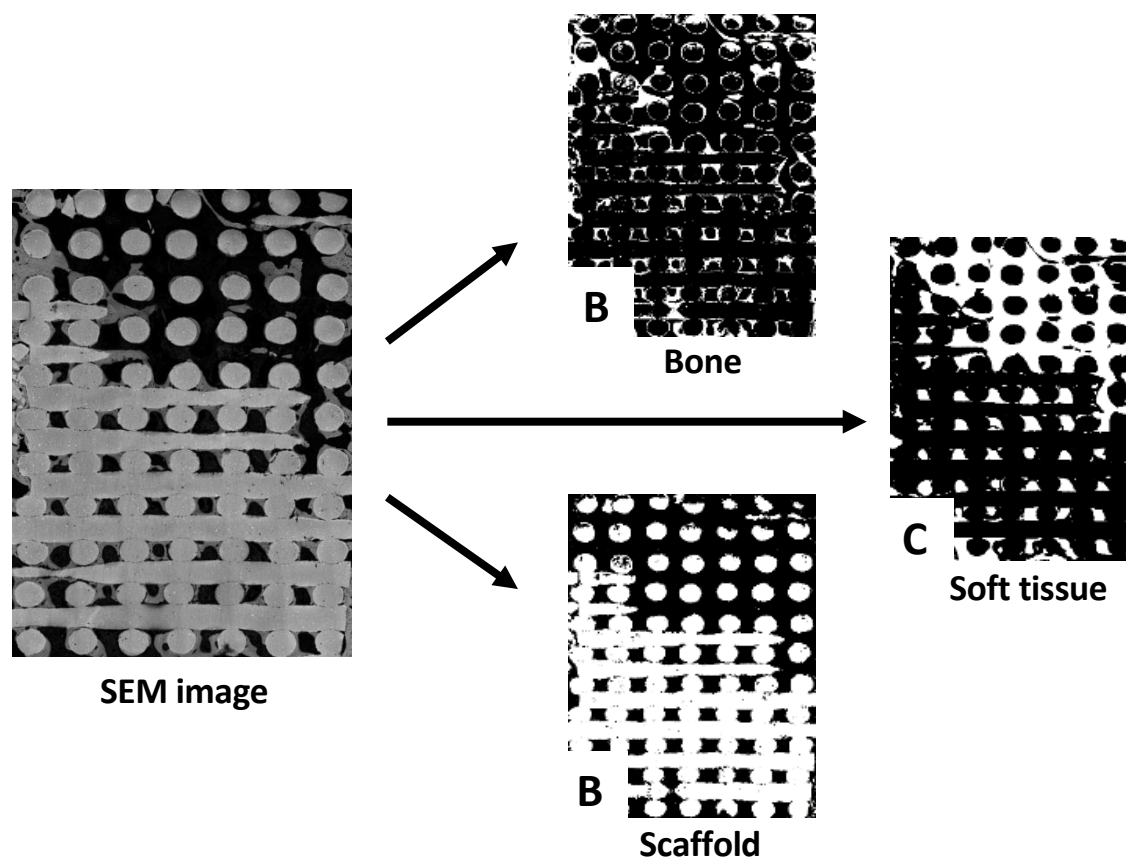
Figure 4 : Results of the segmentation of SEM cross-section image

The comparison with the micro-CT image allows the definition of an objective threshold. The same cross section was reached between the SEM images (Figure 5.B) and the µCT-3D reconstruction (Figure 5.A) with the software Nrecon (Micro photonics inc). The spatial resolution is clearly higher in the SEM cross section than the µCT, which permits to access the bone formation with more precision. In addition, the contrast resolution is also considerably better in the SEM image which potentially allows us to determine the goodness of fit of a segmentation model applied to the µCT image stack. Subtle differences can be noticed between both images, due to the limits of reorientation with the software Dataviewer (3DSuite software, Bruker), shows the limits of this method.
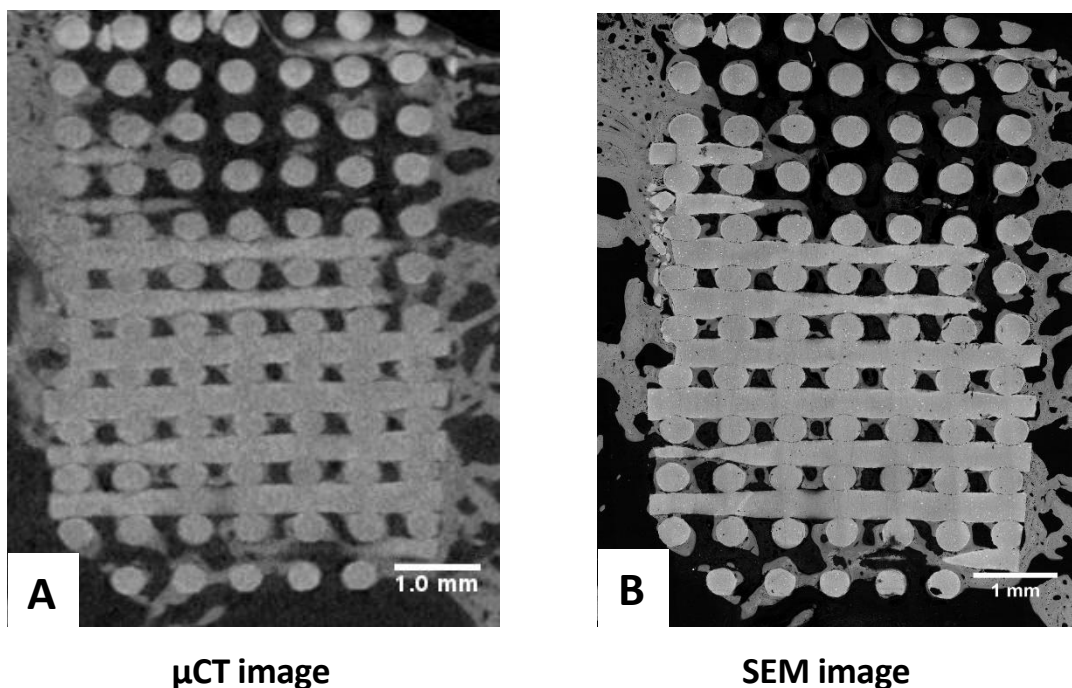
µCT image   **SEM image**

Figure 5 : same cross section of SEM images and µCT reconstruction

Finally, the integrity of the 3D reconstruction by micro-CT is analysed with these parameters with CTan software (3DSuite software, Bruker) and permits the separation of bone, scaffold and the rest present in all the scaffold. This method comes from an earlier study aimed at reducing subjectivity in the analysis of micro-CT data. [26]

3.5. Statistical analysis

When possible, the results are presented as mean values ± standard error. Minitab statistical software (Minitab, LLC) was used for statistical analysis. Statistical significance was defined as $p < 0.05$. Statistical comparisons among experimental groups were performed using one-way repeated measures ANOVA followed by Tukey's post hoc test. A pair-wise comparison result of $p < 0.05$ was considered statistically significant.

4. Results and discussion

4.1. Raw material characterization

SEM images of the α-TCP powder obtained for the powder before and after sieving down to 40µm are shown in Figure 6. No difference is visible between the two conditions, with a particle size of less than 5µm and a coarse circular morphology. The initial particle size of the α-TCP powder is much smaller than the 40µm sieve size, which explains the similarity of the two conditions. The use of a 40µm sieve is therefore not a necessity but ensures that no undesirable particles larger than 40µm are present.
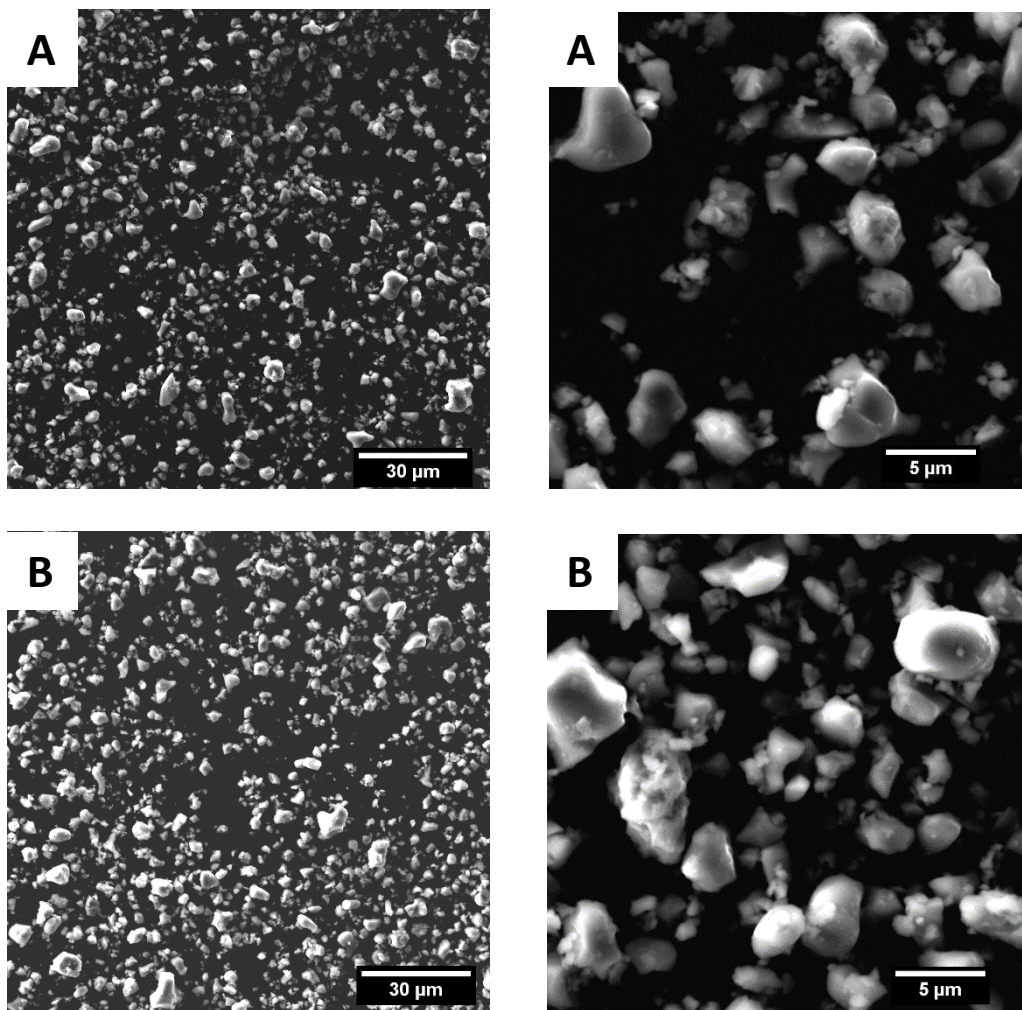

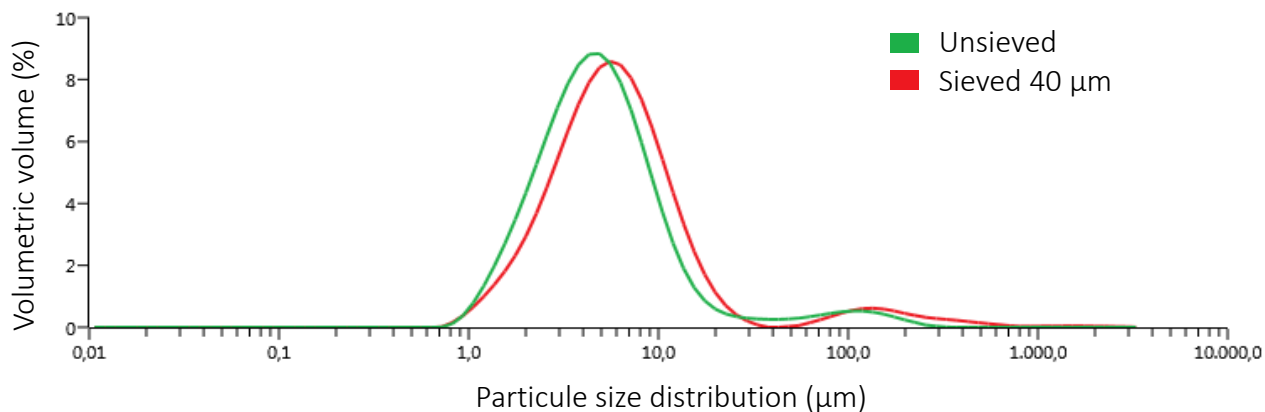*Figure 6 : α-TCP powder (A) unsieved and (B) sieved*

Figure 7: Particule size distribution of the α-TCP powder sieved and unsieved

No significant difference is obtained in the PSD analysis (Figure 7). Indeed, the sieved powder has an average of 5.52μm while the unsieved has an average of 4.62μm. This difference can be explained by the fact that the powder agglomerates in the solvent. As the times in the solvent may change slightly between two experiments, this could explain this slight difference. The secondary peak observed on the right of the graph seem to be due to bubbles present during the experiment and distorting this part of the results. The fact that this secondary peak is present in the case of sifted powder confirms this observation. No additional peaks are visible above 40μm for the unsieved sample. This result suggests that the powder obtained after processing does not have particles larger than 40μm. However, sieving remains a necessary step to prevent the print head from clogging.

In Figure 8 representing the results of the XRD analysis, all the peaks identified in the diffractogram correspond to the pattern of α-TCP (ICDD PDF 00-029-0359).
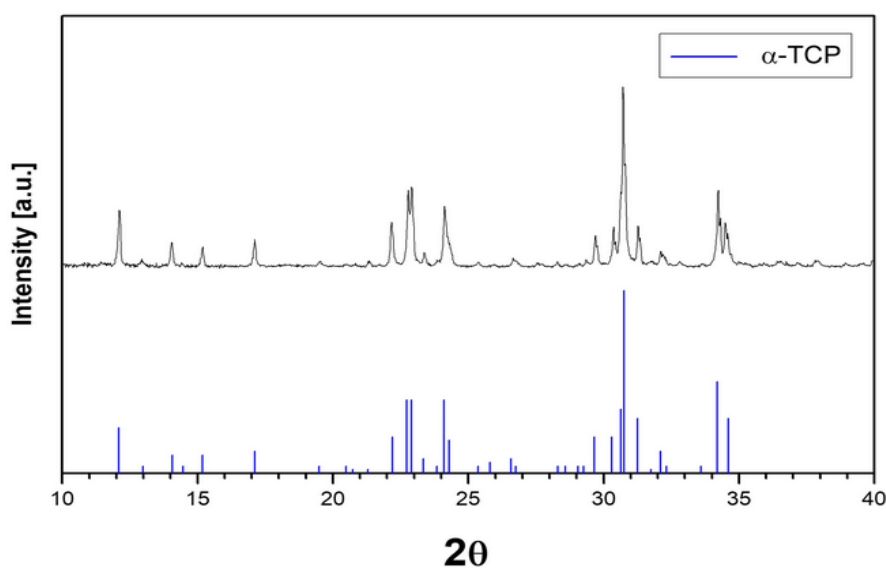

Figure 8 : X-ray diffractogram of the () powder raw material. Characteristic peaks of the three cristalline phases identified in the material represented in the bottom of the figure

4.2. Scaffolds characterization

4.2.1. Chemical

The composition obtained for each condition of scaffold was determined by X-ray diffraction and is summarised in the table 4. CDHA was the main phase in the three conditions, with a 100% for the biomimetic treatment. The presence of β-TCP is also observed with the hydrothermal treatment, with 5.5% for the cylindrical condition and 7.7% for the no cylindrical one. This values are in agreement with the results found in previous research for scaffolds manufactured under similar conditions [8] . Furthermore, no presence of unreacted α-TCP is observed for any condition. In the Figure 9 we can compare the diffractograms of the three sample conditions. We observe how the peaks of samples hardened under hydrothermal treatments (H-C and H-NC) present sharper peaks than the biomimetic one (B-C); This indicates a higher crystallinity for the hydrothermal treatments.

Table 4. Crystalline phase composition of each sample condition

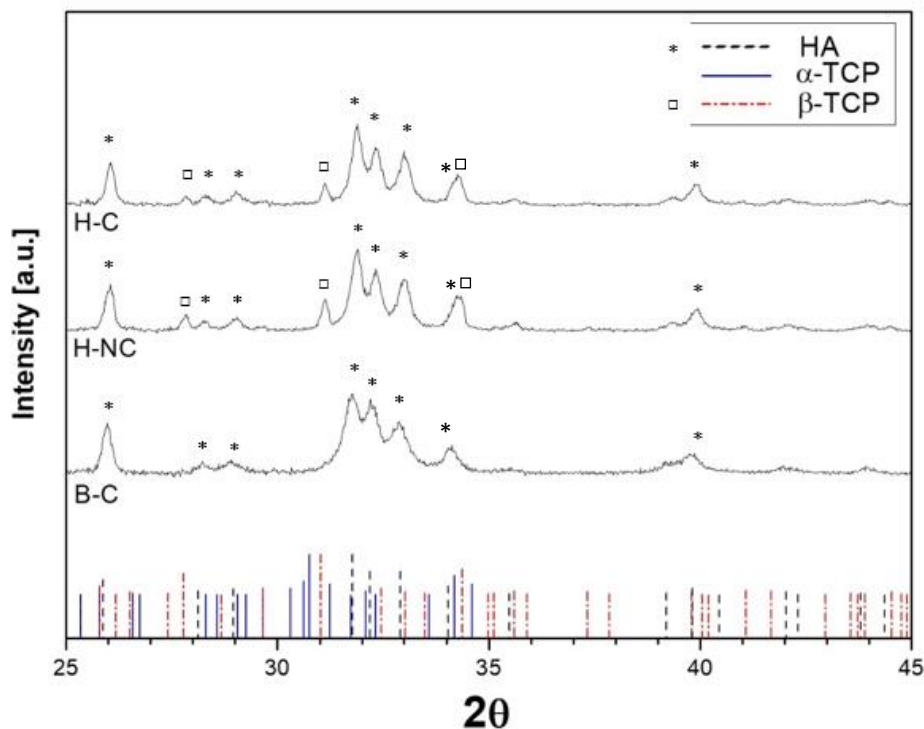|	CDHA	BETA-TCP	ALPHA-TCP
H-C	94.5%	5.5%	0%
B-C	100%	0%	0%
H-NC	92.3%	7.7%	0%

Figure 9. X-ray diffractogram of the different samples conditions. Characteristic peaks of the three crystalline phases identified in the material represented in the bottom of the figure.

The FTIR spectra of the different specimens are displayed in Figure 10. The typical bands characteristic of the different PO4 vibration modes of (v1~980, v2~363, v3~1082 and v4~515 cm-1) [28] present in calcium phosphates were identified in all samples. In addition, no C-H sp3 binding is observed on the FTIR spectra, which means that all samples contain a low level of pluronic. The overlapping of the infrared spectral bands of α-TCP, β-TCP and CDHA made it hard to distinguish them.
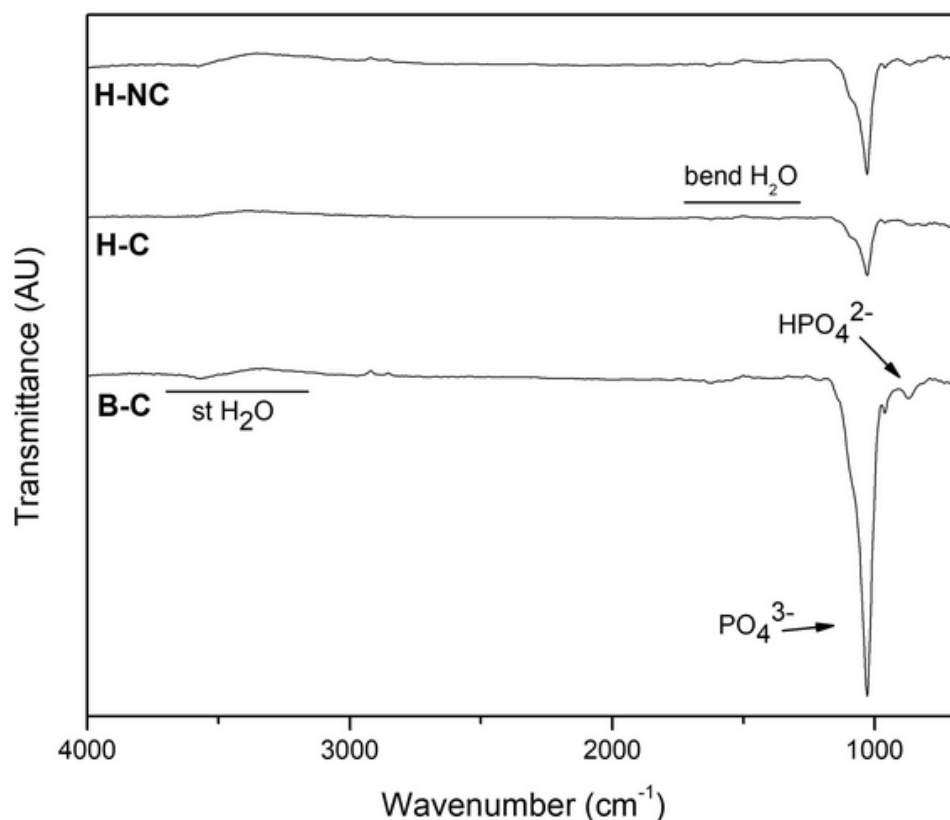
Figure 10 : FTIR spectra of the three conditions: H-NC, H-C and B-C

4.2.2.   Textural

The architecture of the different 3D-printed scaffolds and its microstructure can be seen in Figure 11. The overall architecture of the scaffolds presents great regularity and excellent structural integrity for the three conditions (Figure 8.A, 8.B, 8.C). The scaffolds manufactured under hydrothermal conditions (H-C and H-NC) present a similar microstructure consisting of an entangled network of needle-like CDHA nanocrystal (Figure 8.G, 8.I, 8.J and 8.L), whereas the microstructure of the scaffolds manufactured under biomimetic conditions consists of plate-like CDHA nanocrystals (Figure 8.H and 8.K).   This results in a higher SSA for the B-C with 38.54 m²/g compared to both "hydrothermal" scaffolds that present a similar SSA, with 27.11 m²/g for H-C and 26.55 m²/g H-NC.
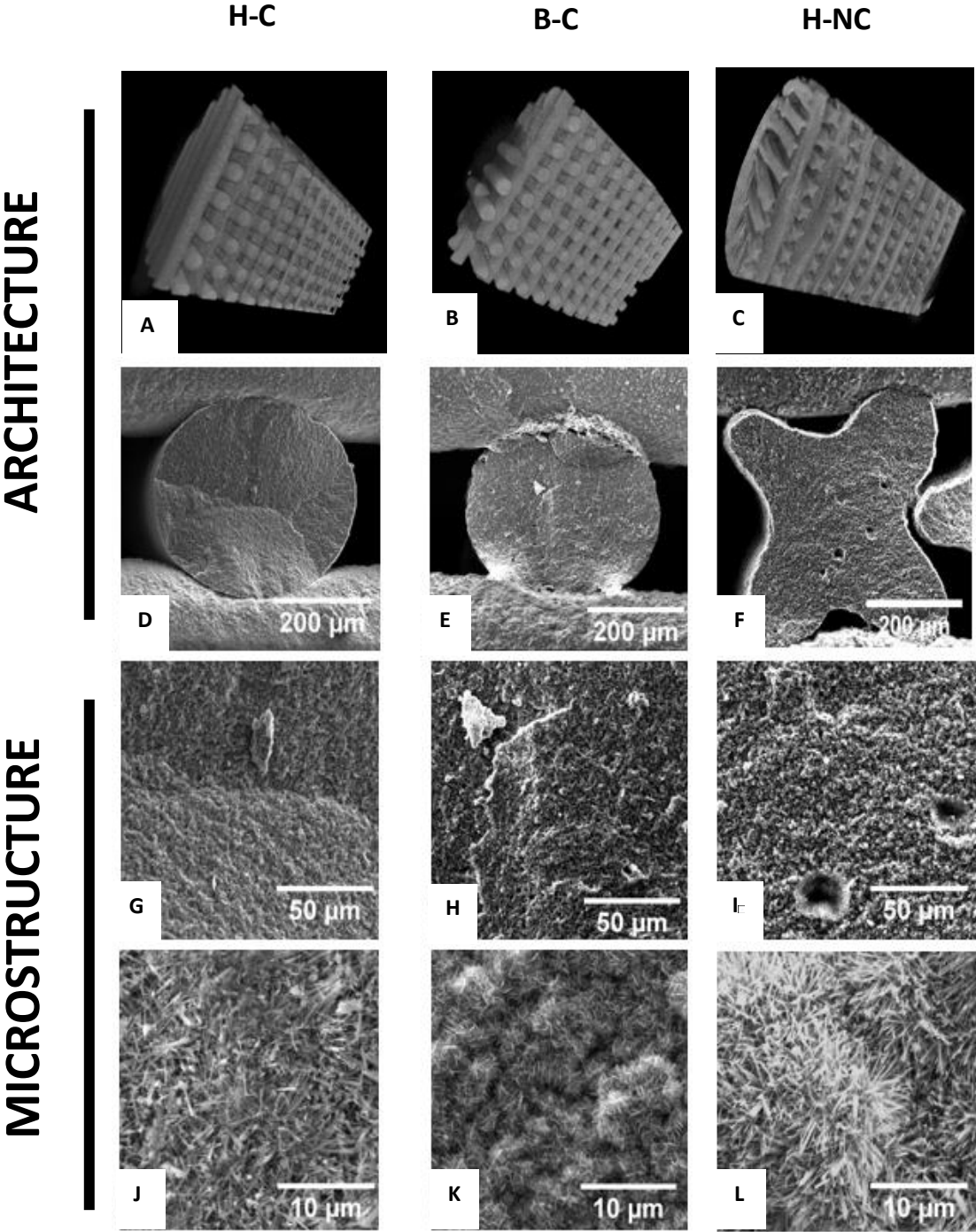
Figure 11. Architecture and microstructure of H-C, H-NC, and B-C in µCT (A,B and C) and SEM (D,E,F,G,H,I,J,K and L)

The pore size distribution, measured by MIP, is shown in the Figure 12. The three conditions show similar bimodal pore distribution with a peak at high pore entrance sizes corresponding to the intrer-strand macropores and a second peak at lower pore entrance size corresponding to the intra-strand microspores. We observe that the microporosity peak presents a shift to the left for the scaffolds manufactured in biomimetic conditions.

This indicates a smaller pore range: 0.006 µm to 0.09 µm for the biomimetic compared to 0.01 µm to 0.1 µm for the hydrothermal conditions. This result is directly correlated with the differences observed in the microstructure and the SSA in these two conditions. Despite we notice differences in the relative heights of the peaks in the micropore range, we cannot extract conclusions from these observations because, due to the nature of the logarithmic plot, this differences correspond to very small changes in the porosity percentage as they correspond to low values of pore entrance size. In addition, we cannot rely on the differences in height observed in the macropore peaks because part of the porosity distribution in the samples is out of the machine measure range (0.006 – 360 µm).
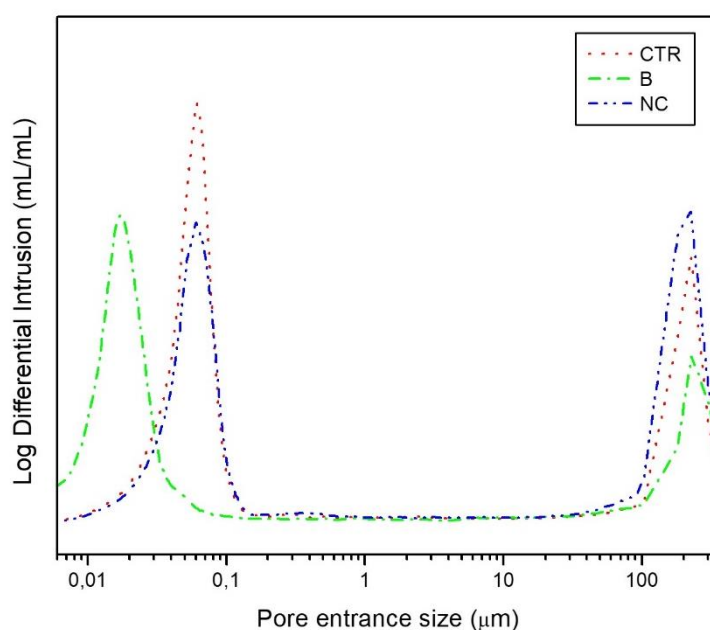

Figure 12 : MIP results (pore entrance size vs log differncial intrusion) for H-C, H-NC, B-C

The apparent density of the two cylindrical conditions are similar (p>0.05) with 0.74 g/cm³ for H-C and 0.76 g/cm³ for B-C (Table 6). The non-cylindrical condition has a lower apparent density which is significantly different (p>0.05), with 0.65 g/m³. The geometry of the filament has a direct influence on the apparent density. This is directly related to the print parameters set during the design stage of the scaffold

The porosity of the scaffolds, shown in the table 5 and Figure 13, was divided in two categories: the microporosity which corresponds to pores smaller than 10 µm and the macroporosity corresponding to pores larger than 10 µm. Both methods for calculating the macroporosity give similar results but without a clear trend. The difference in porosity

between the two cylindrical conditions printed with the same parameters may be explained by the different treatment undergone. In fact, the biomimetic treatment may cause a greater shrinkage of the filaments than the hydrothermal treatment, thus generating a greater macroporosity, but decreasing the total surface of the filaments, explaining a lower microporosity. This impact of the treatment is a strong hypothesis and needs to be verified by complementary studies, in particular with the analysis of the pore size distribution by µCT. The total potosity of the non-cylindrical condition is slightly higher than the cylindrical condition, consistent with the lower bulk density. However, this difference appears to be small (3% to 4%) to reveal a clear trend. In general, the total porosity of the three conditions is close and the distribution between macroporosity and microporosity is similar, as shown in the histogram in Figure 13. This shows consistency in the manufacturing process as well as a viable samples for an in-vivo comparison.

Table 5 : Porosity (micro and macro) obtained by different methods

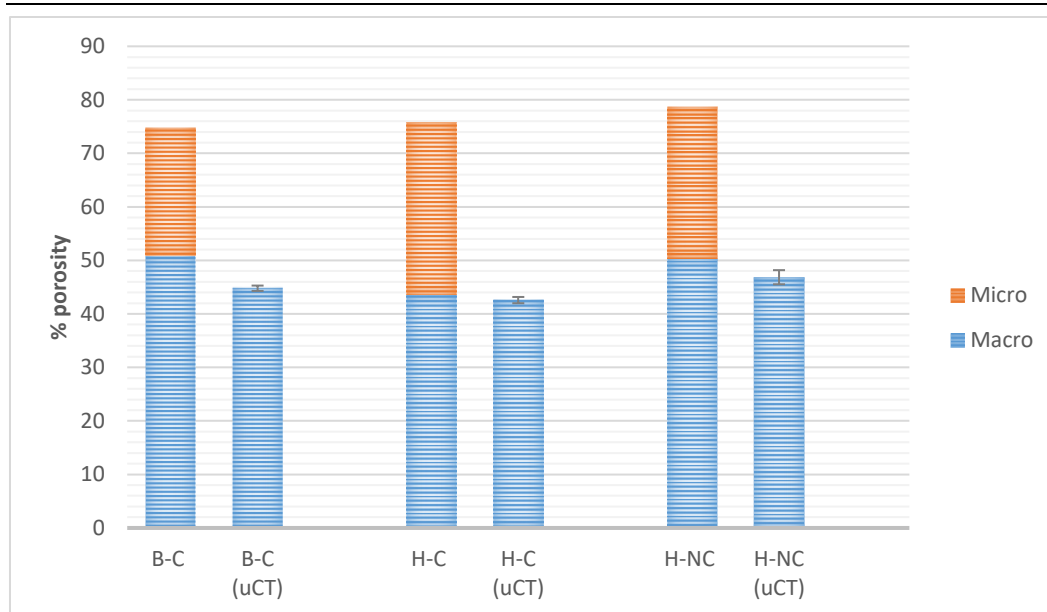| MATERIALS	POROSITY					
	Total porosity (Pycnometer and apparent density)	Macroporosity by micro-CT	Microporosity by MIP (<10um)	Macroporosity (microporosity and total porosity (>10um)	Apparent density (g/cm^3)	SSA (m²/g)
H-C	75.78 %	42.58% ± 0.58%	32.21 %	43.57 %	0.74 ± 0.03	38.54
B-C	74.71 %	44.79% ± 0.5%	23.76 %	50.95 %	0.76 ± 0.06	27.11
H-NC	78.72 %	46.85% ± 1.32%	28.33 %	50.32 %	0.65 ± 0.04	26.55

Figure 13 : Histogram of the porosity of B-C, H-C and H-NC

4.2.3.   Mechanical

The results obtained for the wet compression tests of the polished and unpolished scaffolds and the Weibull modulus associated with each condition are shown in Figure 14.

We observe how the polishing step hinders the compression properties of the scaffold by introducing defaults in the micro-structure that result in a significant reduction of the mechanical properties. Indeed, the results are significantly different ($p<0.05$) for the H-C and B-C conditions. For the H-NC condition, the results are significantly similar, but this can be explained by the low values in this condition. Moreover, two conditions show a decrease in compression behaviour while the B-C condition shows an increase in compression behaviour. This result seems surprising and unexpected. Indeed, the polishing step removes the parts of the scaffold with a higher density that gives an increased resistance to the material.

The H-NC condition shows, in agreement with previous work conclusions [8], an extremely low ultimate compression strength with a value of 1.45 MPa in the unpolished condition. This is explained by the geometry of the filaments: the cylindrical shape of the filaments present a superior compression strength due to the superior inter-filament contact surface, allowing a better distribution of forces and consequently lower tension

concentrations, than with non-cylindrical filaments. In that sense, the geometry of the filament has a direct influence on the scaffold compressive strength and a cylindrical geometry presents a better structural performance.

The influence of the treatment on the mechanical properties has been analyzed with the unpolished samples. Indeed, the polishing step induces an additional intervention that may cause defects, whereas the unpolished scaffolds have the same structure and can be compared. The biomimetic treatment gives structural properties inferior to those given by the hydrothermal treatment. In addition, the Weibull modulus is higher in the unpolished case, with the exception of B, but this result seems surprisingly counter-intuitive. The non-polishing of the scaffold allows for better reproducibility of the mechanical properties and better reliability. This results are in agreement with the findings of previous works [8] and can be attributed to the differences observed in the microstructure.
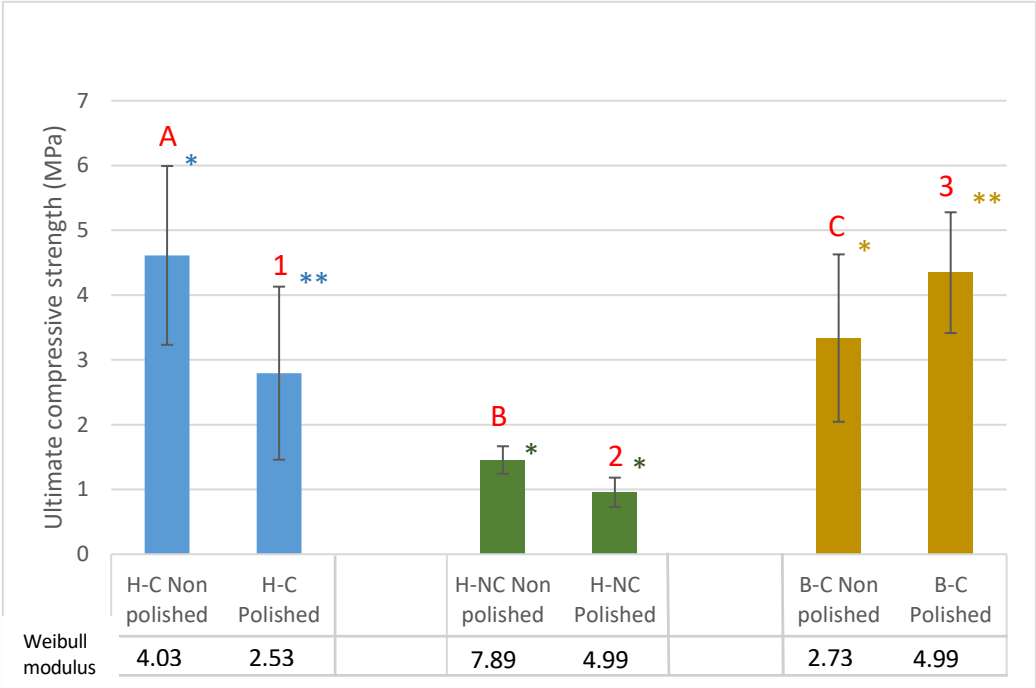

Figure 14 : Ultimate compressive strength in wet condition for the 3 conditions scaffold in two state, polished and non polished. Groups identified by the same symbol are not statistically different (p>0.05) (Letter for the non polished group, number for the polished groups and asterisk of the same colour for the same condition)

4.3. In vivo results

4.3.1. Histomorphometrical assessment

4.3.1.1. 2D analysis

The 2D analysis (Figure 15) shows the percentage of bone formed in the available area. This allows the images to be compared with each other since the amount of scaffold, which varies according to the cutting angle, is removed. The error bars in Figure 15 represent the standard error of the mean. Indeed, the number of samples that could be analysed varies according to the conditions, and this treatment allows to compare them. (5 for H-C, 3 for B-C and 3 for H-NC). The results are very similar for the three conditions, with 35% for biomimetic condition, 30% for H-C and 28% for H-NC. This shows that hydrothermal or biomimetic treatment seems to have the same effectiveness on bone formation. The same is true for the geometry of the filaments, the cylindrical or non-cylindrical shape have the same impact on bone formation. In this context, the performance of the scaffolds is maintained, whatever the treatment or the shape of the filaments. However, this analysis considers only a section of the scaffold and not the entire volume. This interpretation must therefore be complemented by 3-dimensional analysis.
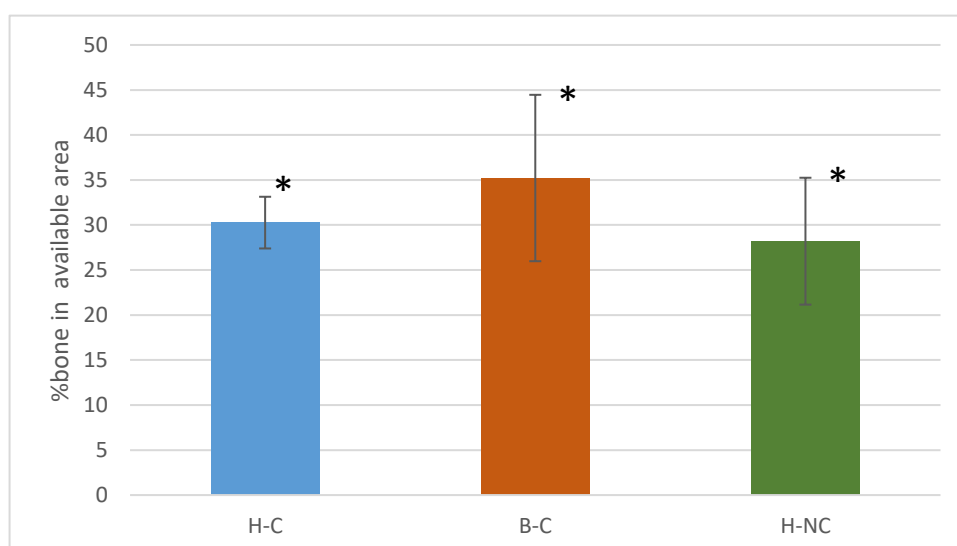

Figure 15 : Histogram of the percentage of bone formation in the available area. Bars indicate standard deviation. Groups identified by the same symbol are not statistically different (p>0.05)

4.3.1.2. 3D analysis

The 3D analysis had difficulties in separating the 3 phases. Indeed the µCT reconstruction shows two main problems:

- The slight difference of grey scale between the bone and the scaffolds which made hard to difference them even with the SEM references. In the histogram of grey scale Figure 16. A, two pics are visible. The first one from 10 to 40 represents the resin part, the second one from 90 to 120 is composed of the bone and the scaffolds. It shows the difficulty to separate the two entities. It can be explained by the similar composition of the bone and the scaffold. Indeed, the mineral phase of bone is composed of phosphate calcium such as the scaffolds.

- The evolution of the grey scale of the same parts in different part of the µCT reconstruction. The Figure 16 shows two parts of the same scaffold obtained by µCT reconstruction. The evolution of the grey scale of the scaffolds is important, going from 95 to 115. The Figure 16.B illustrates this evolution in the same cross section, with a difference of 15 on the grey intensity. This evolution impacts directly the treatment of all the µCT reconstruction. Indeed, the thresholds are fixed according to one cross section and appears obsolete in other part of the scaffold.
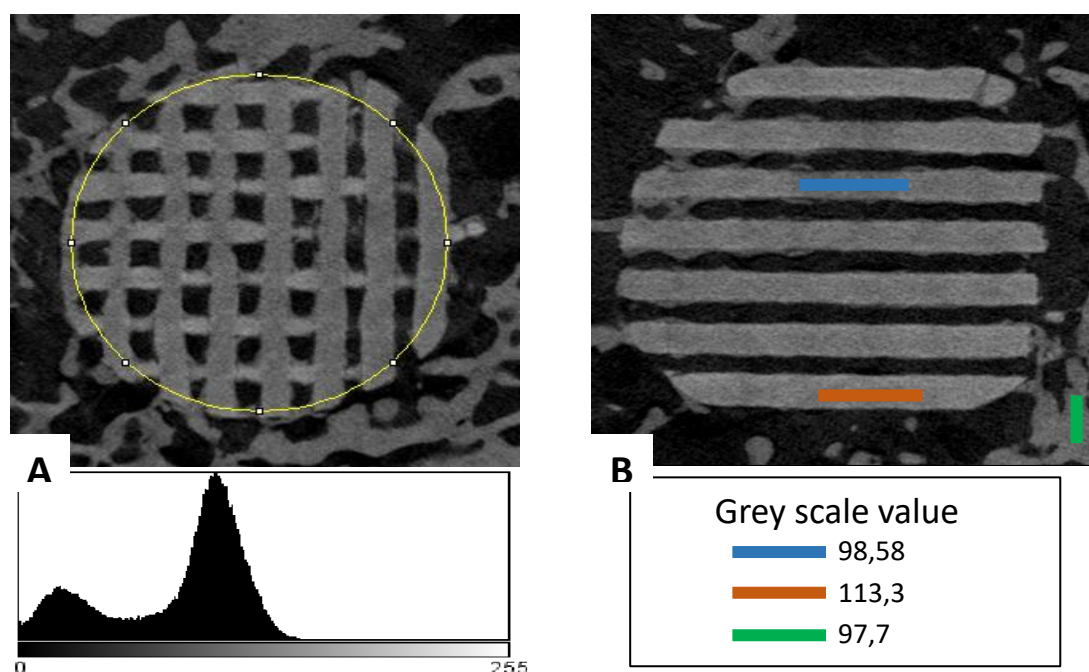
Figure 16 : Grey scale analysis: ROI histogram (A) and evolution of grey intensity (B)

4.3.2. Histological assessment

Two imaging techniques were used for the characterization of the histological cuts: SEM stitchings and Goldner-Masson-trichrome staining. Images of the same conditions at different magnifications do not necessarily come from the same sample.

In the SEM images (Figure 17, 18 and 19), bone and biomaterial could be distinguished and evaluated due to their differences in terms of gray-scale intensity and texture. Whilst bone tissue exhibits lower gray values and presents a lamellar structure with circular osteons and osteocytes entrapped in the center, the biomaterial gray values are slightly higher and have a less oriented noise-like texture. Inside the biomaterial we can observe black pores, 10 to 15 µm, that correspond to small bubbles entrapped in the pasty ink during the fabrication process. In addition, for the structures manufactured on hydrothermal conditions, we observe some white inhomogeneity that could correspond to the β-TCP present in the composition of these samples.
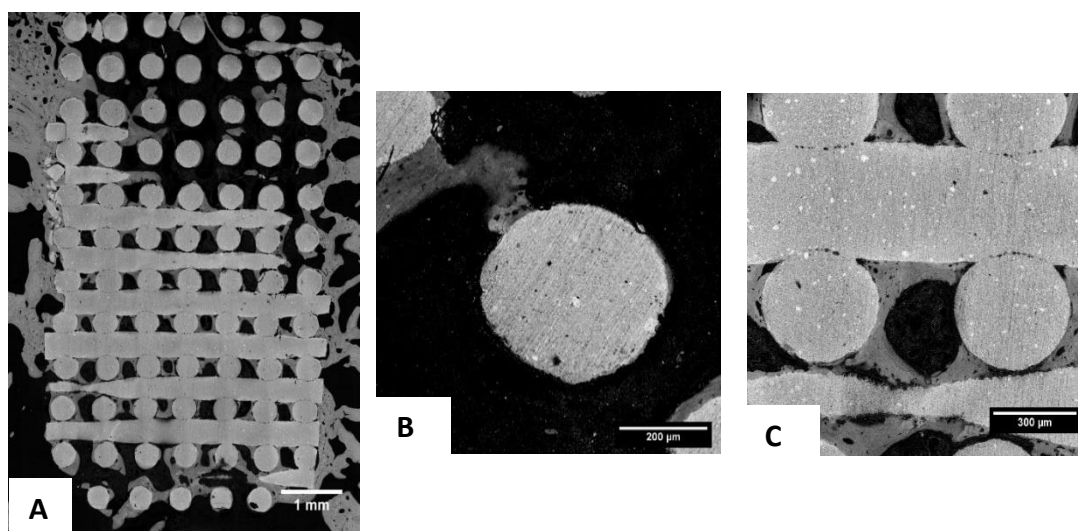

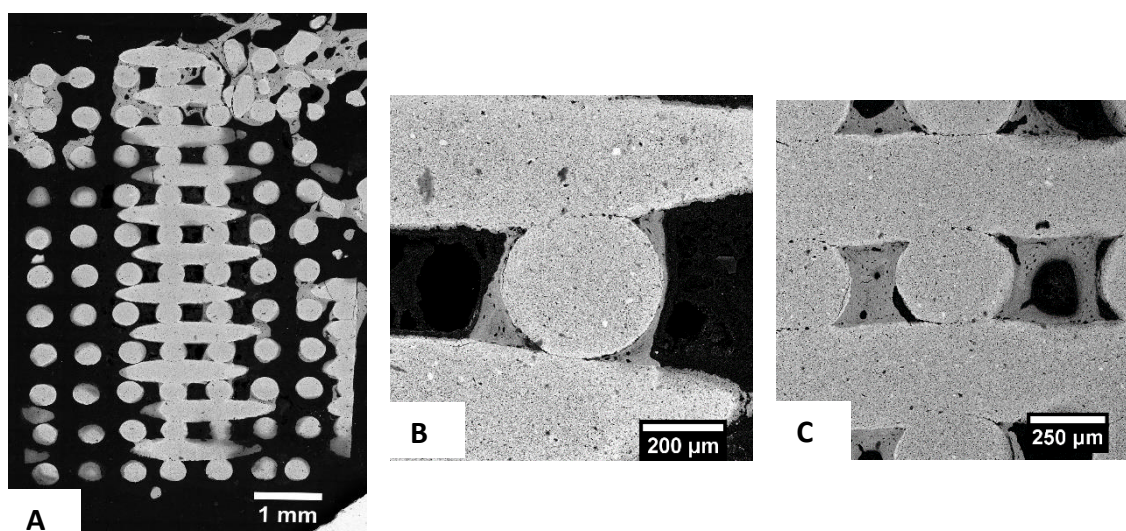*Figure 17 : SEM images for H-C condition: General view (A) and details (B)(C)*

Figure 18 : SEM images for B-C condition: General view (A) and details (B)(C)
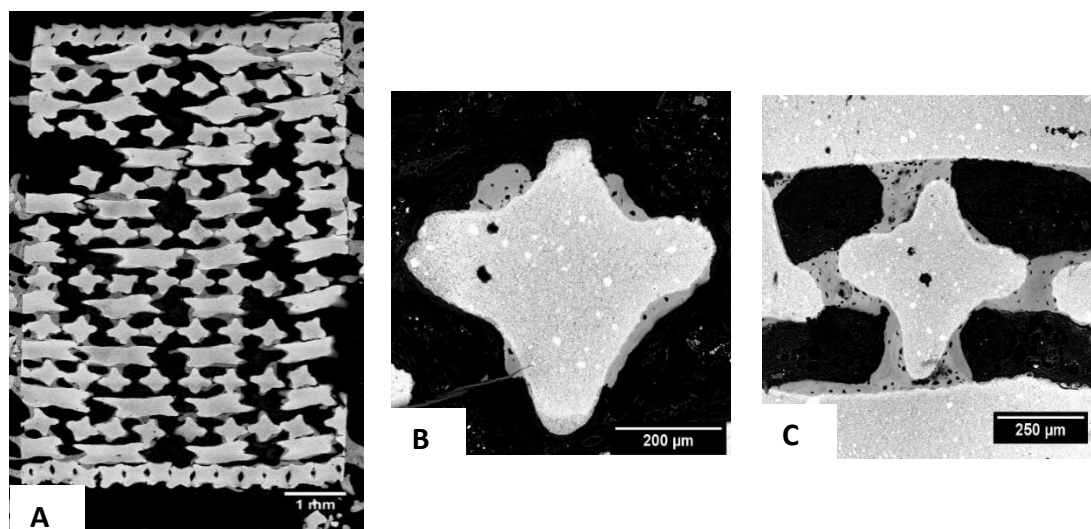
Figure 19 : SEM images for H-NC condition: General view (A) and details (B)(C)

In the Goldner-Masson-trichrome stainings of the samples we can observe (Figure 20) the mineralised tissue (asteriks) stained in green and the bone graft (BG) without any staining (or slightly in green). In the high magnification images we can also distinguish the lamellar structure of the new formed bone.

Both imaging techniques revealed the presence of new bone formation with a morphology consisting of a mixture of woven bone and some areas of well-organized lamellar bone following a Haversian pattern, similar for all groups.

All the sample groups presented a successful osteointegration of the scaffold. No signs of fibrous tissue (stained in brown/red) encapsulating the bio-material could be observed in the stained samples. The stained sections show a widespread blood vessel (black arrows) network, from small capillaries to medium size vessels, within the macropores of all three scaffolds. The images indicate that in most cases the mineralization process starts in the concave surfaces of the scaffolds. And this phenomenon not only occurs in the non-cylindrical-strands condition but also in the cylindrical scaffolds, where the bone starts mainly growing in the intersection of strands. This is why we see a higher thickness of bone corresponding to a higher number of mineralization layers. The structure of the new formed is very similar appearance to that found in the surrounding trabecular bone (Figure 21) consisting in a highly porous structure with a high inter-connectivity. It was not possible to qualitatively distinguish a higher level of osteoconduction or osteoformation for any of the conditions. However the qualitative results indicate a slightly higher amount of bone for the B-C scaffolds (obtained from 2D results that are

highly subjective and dependent on the slice orientation with regards to the scaffold structure).
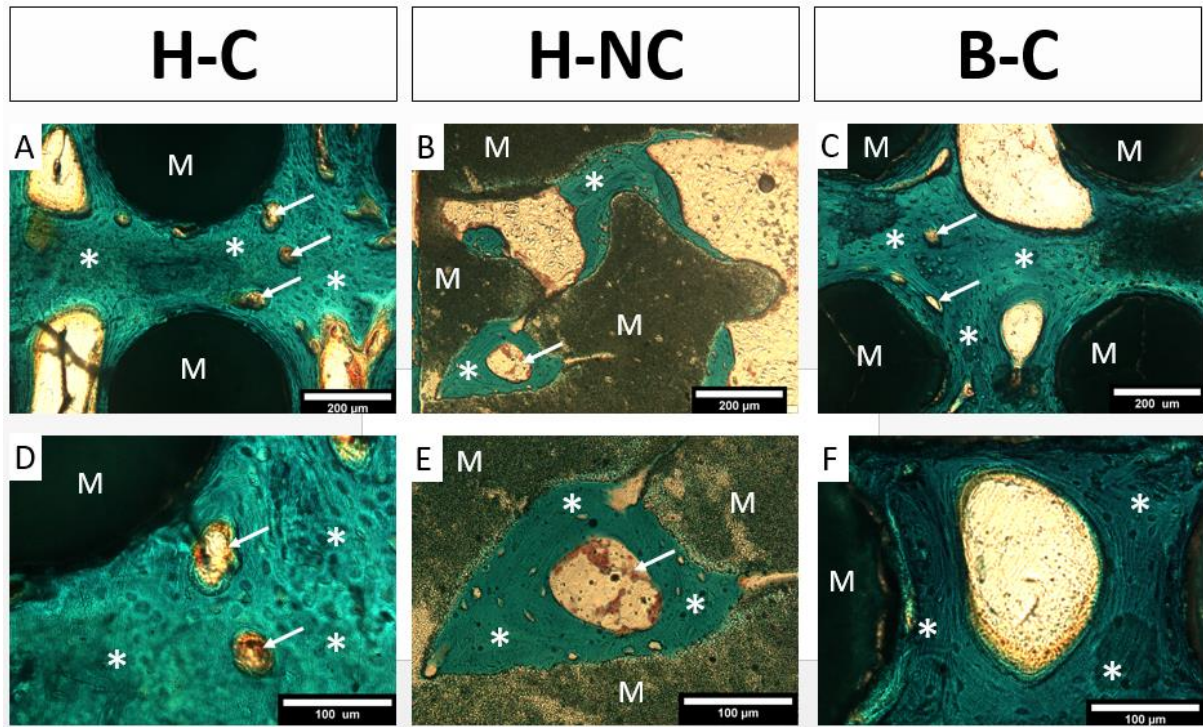
Figure 20 : Analysis of cross section after Goldner-Masson Trichrom stained for the H-C, H-NC and B-C conditions. Images were processed at different magnifications; x20 for A,B and C; x50 for D,E and F. (M) is material (scaffold), (*) is the new bone matrix organised in haversian structures and white arrows are blood vessel. Osteocytes can be seen as small in the bone matrix.
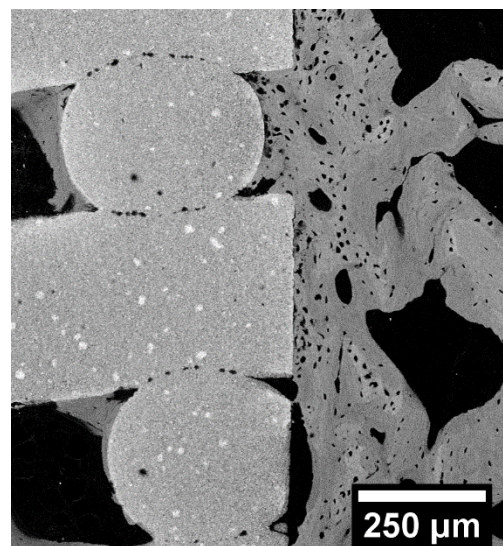

Figure 21 : SEM images for H-NC condition: General view (A) and details (B)

5. Conclusion

From this study we conclude that the hydrothermal treatment and the traditional hardening biomimetic routes have strong similarities. The scaffolds obtained by these two processes have similar characteristics such as porosity and mechanical properties. Only the microstructure differs significantly, with a needle like structure for the hydrothermal route and a flat like structure for the biomimetic route, thus modifying the specific surface area. Also the composition presents significant differences with the apparition of an additional allotropic phase in the chase of hydrothermal treatments. On the *in vivo* analysis, despite the missing analysis of the quantity of bone generated over the entire volume of the scaffolds for technical concerns, the qualitative analyses of the SEM images and histology does not show significant differences on the quantity of bone, morphology and, more generally, in vivo performance between the two conditions. Under both conditions, the closed microenvironment present at the intersection of filaments are preferential areas where bone seems to have more affinity to grow. The hydrothermal routes therefore seems to be a good alternative to the traditional biomimetic routes, allowing considerable time savings during manufacture which can be of high impact for its translation to the industry. A process including the hydrothermal treatment would be more competitive and attractive to fulfill the fast delivery requirements of a patient-specific product required on medical emergencies.

We can also conclude from this study that, despite a change in the strand geometry, the main characteristics, such as the porosity percentage, microstructure and composition, are identical to the pristine sample hardened with the same hydrothermal treatment. The change of porosity shape during the design stage allowed to keep a similar total porosity. Only the mechanical behaviour is substantially hindered by this change in filament shape, due to a less balanced distribution of forces. This change in mechanical properties was the cause of problems during the implementation of the scaffolds. This property is therefore likely to be improved. The non-cylindrical shape, with the manufacturing conditions present in this project, is therefore a comparable alternative to the classical cylindrical shape. Contrary to the results obtained in Barba's project[13], the concavity present in our scaffold is only partial. With a rectilinear printing pattern it is not possible to obtain concavities in all the directions like it appends in foamed and litched scaffolds. The morphology is therefore different from the foams studied in the Barba project, the concavity is less present in the current case. The 3D analysis could not be completed

and only 2D quantitative analyses were carried out. The concave zone of the filaments as well as the intersection of the filaments seems to favour the formation of new bone, acting as a microenvironment favouring the formation of new bone.

This project allows a new vision on the fabrication of scaffolds by robocasting for bone generation, since it introduces the influence of filament geometry and of treatment in bone formation. However, the technical difficulties concerning the volume segmentation of the samples limits the analysis of this influence. This study is therefore conducted to be complemented by other image analysis tools, in particular with image processing prior to segmentation, making it possible to compensate for grey level variation.

Economic analysis

Table 6: Summary of the economical dispenses on sample characterization

TECHNIQUE	UNIT PRICE (€/H)	TIME PER SAMPLE (MIN)	Nº SAMPLES	COST (€)
MICRO -CT	18	283	18	1528
HE PYC	-	-	4	52
DESKTOP SEM	9	65	18	175.5
MIP	-	-	3	393
BET	-	-	3	261
TOTAL				**2 251.5 €**

Table 7: Summary of the economical dispenses on sample preparation

ARTICLE	UNIT PRICE (€/UT.)	UNIT TYPE	Nº UNITS	COST
TECNOVIT	490	L	1	490
SANDPAPER	1.5	UT	35	52.5
ETHANOL	23	L	5	115
ACETONE	30	L	0.5	15
ABS. ETHANOL	40	L	3	120
30 ML PP CONTAINER	0.28	UT	60	16.8
PARAFILM	0.5	m	2	1
GLOTHES	0.04	UT	300	12
TOTAL				**822.3 €**

Table 8: Summary of the economical dispenses on human resources

POSITION	UNIT PRICE (€/H)	QUANTITY (H)	COST
PROJECT DIRECTOR	60	20	1200€
PHD STUDENT	30	200	6 000€
LAB MANAGER	60	15	900€
SALARY	12	600	7200€
TOTAL			**15 300€**

Ecological aspect

Different chemicals with a high environmental impact were used in this project. First of all formalin, with corrosive, mutagenic, carcinogenic and toxic properties. The Technovit 7200 resin used also has a high environmental impact with toxic and dangerous properties for aquatic environments. Finally, the last product with a high environmental impact used in this project is mercury, with mutagenic, carcinogenic, toxic and dangerous properties for aquatic environments. These products were used, sorted and recycled to reduce their environmental impact. Generally speaking, all the solutions used were sorted according to their nature. Similarly, the materials used in this project were sorted according to their nature (organic waste, paper, plastic or household waste) to limit their impact.

The project required resources of different types with varying degrees of environmental impact. Energy resources, exclusively electrical, were necessary for the operation of the many machines used in this project. The cutting and polishing stages involved significant water consumption. These resources were used with care and limited to the maximum.

References

[1] J. . Schmitz, J.P., &Hollinger, "No Title," *Crit. size defect as an Exp. Model craniomandibukofacial nonunions*, vol. clinical o, 1986.

[2] "Biocompatibility | definition of biocompatibility by Medical dictionary." [Online]. Available: https://medical-dictionary.thefreedictionary.com/biocompatibility. [Accessed: 21-Oct-2019].

[3] A. Seth Greenwald, S. D. Boden, V. M. Goldberg, Y. Khan, M. T. Cato Laurencin, and R. N. Rosier, "This material was first published, in slightly different form," *J. Bone Jt. Surg.*, vol. 83, pp. 98–103, 2001.

[4] H. Petite, "La bio-ingénierie de la régénération osseuse," *Medecine/Sciences*, vol. 18, no. 10, pp. 995–1002, 2002.

[5] A. E. Duguy N, Petite H, "No Title," *Biomater. osseous Regen.*, 200AD.

[6] C. P. Cements, C. O. F. Porosity, U. S. E. As, L. Drug, and D. Devices, "Calcium Phosphate Cements and Foams Characterization of Porosity and Use As Local Drug Delivery Devices," 2015.

[7] R. Dwivedi *et al.*, "Polycaprolactone as biomaterial for bone scaffolds: Review of literature," *J. Oral Biol. Craniofacial Res.*, vol. 10, no. 1, pp. 381–388, 2020.

[8] S. Raymond *et al.*, "Accelerated hardening of nanotextured 3D-plotted self-setting calcium phosphate inks," *Acta Biomater.*, vol. 75, pp. 451–462, 2018.

[9] W. Habraken, P. Habibovic, M. Epple, and M. Bohner, "Calcium phosphates in biomedical applications: Materials for the future?," *Mater. Today*, vol. 19, no. 2, pp. 69–87, 2016.

[10] G. Hannink and J. J. C. Arts, "Bioresorbability, porosity and mechanical strength of bone substitutes: What is optimal for bone regeneration?," *Injury*, vol. 42, no. SUPPL. 2, pp. S22–S25, 2011.

[11] B. Wopenka and J. D. Pasteris, "A mineralogical perspective on the apatite in bone," *Mater. Sci. Eng. C*, vol. 25, no. 2, pp. 131–143, 2005.

[12] M. P. Ginebra, M. Espanol, E. B. Montufar, R. A. Perez, and G. Mestres, "New processing approaches in calcium phosphate cements and their applications in regenerative medicine," *Acta Biomater.*, vol. 6, no. 8, pp. 2863–2873, 2010.

[13] A. Barba *et al.*, "Osteoinduction by Foamed and 3D-Printed Calcium Phosphate Scaffolds: Effect of Nanostructure and Pore Architecture," *ACS Appl. Mater. Interfaces*, vol. 9, no. 48, pp. 41722–41736, 2017.

[14] A. Barba *et al.*, "Osteogenesis by foamed and 3D-printed nanostructured calcium phosphate scaffolds: Effect of pore architecture," *Acta Biomater.*, vol. 79, pp. 135–147,

2018.

[15]   K. Kurashina, H. Kurita, Q. Wu, A. Ohtsuka, and H. Kobayashi, "Ectopic osteogenesis with biphasic ceramics of hydroxyapatite and tricalcium phosphate in rabbits," *Biomaterials*, vol. 23, no. 2, pp. 407–412, 2002.

[16]   P. Habibovic, H. Yuan, C. M. Van Der Valk, G. Meijer, C. A. Van Blitterswijk, and K. De Groot, "3D microenvironment as essential element for osteoinduction by biomaterials," *Biomaterials*, vol. 26, no. 17, pp. 3565–3575, 2005.

[17]   A. Diez-Escudero, M. Espanol, S. Beats, and M. P. Ginebra, "In vitro degradation of calcium phosphates: Effect of multiscale porosity, textural properties and composition," *Acta Biomater.*, vol. 60, pp. 81–92, 2017.

[18]   A. Kumar *et al.*, "Low temperature additive manufacturing of three dimensional scaffolds for bone-tissue engineering applications: Processing related challenges and property assessment," *Mater. Sci. Eng. R Reports*, vol. 103, pp. 1–39, 2016.

[19]   Y. Maazouz *et al.*, "Robocasting of biomimetic hydroxyapatite scaffolds using self-setting inks," *J. Mater. Chem. B*, vol. 2, no. 33, pp. 5378–5386, 2014.

[20]   W. Kim *et al.*, "An innovative cell-laden a-tcp/collagen scaffold fabricated using a two-step printing process for potential application in regenerating hard tissues," *Trans. Annu. Meet. Soc. Biomater. Annu. Int. Biomater. Symp.*, vol. 40, no. February, p. 883, 2019.

[21]   K. A. Soliman, K. Ullah, A. Shah, D. S. Jones, and T. R. R. Singh, "Poloxamer-based in situ gelling thermoresponsive systems for ocular drug delivery applications," *Drug Discov. Today*, vol. 24, no. 8, pp. 1575–1586, 2019.

[22]   Y. Maazouz, E. B. Montufar, J. Malbert, M. Espanol, and M. P. Ginebra, "Self-hardening and thermoresponsive alpha tricalcium phosphate/pluronic pastes," *Acta Biomater.*, vol. 49, pp. 563–574, 2017.

[23]   R. B. Rao, K. L. Krafcik, A. M. Morales, and J. A. Lewis, "Microfabricated deposition nozzles for direct-write assembly of three-dimensional periodic structures," *Adv. Mater.*, vol. 17, no. 3, pp. 289–293, 2005.

[24]   E. Edition, *Guide for the Care and Use of Laboratory Animals*. Washington, D.C.: National Academies Press, 2011.

[25]   "Directive 2010/63/EU of the European Parliament and of the Council of 22 September 2010 on the Protection of Animals Used for Scientific Purposes." .

[26]   S. Lewin, A. Barba, C. Persson, J. Franch, M. P. Ginebra, and C. Öhman-Mägi, "Evaluation of bone formation in calcium phosphate scaffolds with μCT-method validation using SEM," *Biomed. Mater.*, vol. 12, no. 6, pp. 1–21, 2017.

[27]   D. Pastorino, C. Canal, and M.-P. Ginebra, "Multiple characterization study on porosity and pore structure of calcium phosphate cements," *Acta Biomater.*, vol. 28, pp. 205–214, Dec.

2015.

[28] V. M. Bhatnagar, "The preparation, X-ray and infra-red spectra of lead apatites," *Arch. Oral Biol.*, vol. 15, no. 6, pp. 469–480, 1970.

Appendix 1 – Implantation process

Operating procedure

All animal procedures in this study were performed in compliance with the Guide for Care and Use of Laboratory Animals [24] and the European Community Guidelines (Directive 2010/63/EU) for the protection of animals used for scientific purposes [25] and under the permission of the local Animal Ethics Committee for Human and Animal Experimentation (Approval # CEAAH 4683).

The study was performed on twelve adult female New Zealand rabbits with a weight range of 4.8–5.5 kg and an age range of 8–12 months and purchased from a professional stock breeder. The animals were housed in individual boxes of two square meters each one and an acclimatization period of two weeks was established prior to surgery.

For surgical procedure, the animals were pre-anesthetised using butorphanol (0.5mg/kg s.c.), midazolam (0.5 mg/kg s.c.) and medetomidine (0.05 mg/kg s.c). Anesthesia was induced with propofol (2 mg/kg i.v) and maintained with inhaled isoflorane (2%) in an oxygen carrier. Both rear limbs were clipped and subsequently scrubbed with chlorhexidine gluconate solution 4% for an aseptic preparation of the surgical field. With the animals in dorsal recumbency and after a small skin incision, the medial aspect of both femoral condyles was exposed by a medial parapatellar incision. Using a 2,5mm drill bit and under copious physiological saline irrigation to avoid thermal necrosis, a monocortical bone defect was performed in the centre point of the medial aspect of the condyle. Afterwards, the defect was enlarged with a 5mm drill bit always under continuous physiological saline irrigation. The length of the defect was fixed approximately in 10mm. Cylindrical scaffolds with a diameter of 4.9mm and a height of 10mm with three different conditions previously described (H-C, B-C, H-NC) were then press-fitted in each bone defect. After assuring the good stability of the implants, the joint capsule, the subcutaneous tissue and the skin were sutured in layers in a routine way.

Once recovered from the anaesthesia, the animals were housed again in the same individual boxes used for acclimatization and allowed to full weight bearing. During the postoperative period, analgesic (buprenorphine: 0,03mg/kg sc per day) and antibiotic (enrofloxcin: 10 mg/kg, bid) treatments were given to the animals for 7 days.

Surgeries were uneventful. However, one of the animals did not fully recovered from the surgery, didn't gained weight and finally died few days after the operation. The rest of animals completed a normal postoperative period without any clinical complication. No signs of infection, wound dehiscence, weight loss, behaviour changes, implant migration or lameness were observed along the postoperative period.

The animals were euthanised two months (8 weeks) after the surgical procedure with an overdose of sodium pentobarbital (160mg/kg/i.v.) according to the legislation of the American Veterinary Medical Association (AVMA). A pre-euthanasia sedation of midazolam (0.50 mg/kg s.c.) and medetomidine (0.05 mg/kg s.c) was used for animal welfare reasons.